Multi-objective optimization of energy efficiency and geomechanical safety in high-temperature aquifer thermal energy storage (HT-ATES) systems based on coupled thermo-hydro-mechanical (THM) analysis

Zhang, Le; Mi, Zerui; Cao, Wenzhuo; Liu, Liyuan; Tas, Luka; Hermans, Thomas

DOI
10.1016/j.energy.2025.137096

Publication date
2025

Document Version
Final published version

Published in
Energy

Energy 332 (2025) 137096

Contents lists available at ScienceDirect

Energy

journal homepage: www.elsevier.com/locate/energy

Multi-objective optimization of energy efficiency and geomechanical safety in high-temperature aquifer thermal energy storage (HT-ATES) systems based on coupled thermo-hydro-mechanical (THM) analysis

Le Zhang [a,b,*], Zerui Mi [a], Wenzhuo Cao [c], Liyuan Liu [d,**], Luka Tas [a], Thomas Hermans [a]

[a] Department of Geology, Ghent University, Krijgslaan 281, Ghent, B-9000, Belgium
[b] Faculty of Civil Engineering and Geosciences, Delft University of Technology, Stevinweg 1, Delft, 2628 CN, The Netherlands
[c] Department of Earth Sciences, Utrecht University, Princetonlaan 4, Utrecht, 3584 CS, The Netherlands
[d] School of Resources and Safety Engineering, University of Science and Technology Beijing, Xueyuan Road 30, Beijing, 100083, China

ARTICLE INFO

Dataset link: https://doi.org/10.4121/5770abff-df68-4e9e-900c-b3add1e3d210

Keywords:
High-temperature aquifer thermal energy storage
Thermo-hydro-mechanical coupling
Sensitivity analysis
Uncertainty quantification
Geomechanical stability

ABSTRACT

This paper introduces a comprehensive thermo-hydro-mechanical (THM) modeling framework tailored for high-temperature aquifer thermal energy storage (HT-ATES) systems. Our framework presents a novel dual-assessment approach that simultaneously evaluates thermal performance and geomechanical stability of HT-ATES systems. The framework combines advanced sensitivity analysis with multi-objective optimization to concurrently boost thermal efficiency and maintain geomechanical safety. The model simulates the cyclic injection-extraction process while capturing the interdependent effects of heat transfer, fluid flow, and mechanical stress evolution. A distance-based Generalized Sensitivity Analysis (DGSA) is applied to identify and rank the most critical parameters influencing system performance and stability, particularly in regions such as the cold well and overlying caprock. Furthermore, surrogate models constructed with eXtreme Gradient Boosting (XGBoost) facilitate a computationally efficient Non-dominated Sorting Genetic Algorithm II (NSGA-II) optimization that investigates the trade-offs between enhancing heat production and minimizing failure risks. Validation against high-fidelity simulations reveals that, compared to a benchmark model with a thermal recovery efficiency of approximately 85% and a caprock slip tendency of 34°, the optimized designs achieve around 88% efficiency and reduce the caprock slip tendency to 29°. These quantitative improvements demonstrate that the proposed framework significantly enhances both energy production and geomechanical stability, offering valuable guidance for the design of robust HT-ATES systems under fixed geological conditions.

1. Introduction

The global transition toward sustainable energy systems has highlighted the importance of energy storage technologies as critical solutions for addressing the misfit in energy supply and demand. Among various energy storage methods, long-term thermal energy storage has proven essential for mitigating seasonal variability, particularly as renewable energy sources like solar and wind continue to dominate the energy landscape [1]. Within this context, underground thermal energy storage (UTES) has emerged as a practical solution, exploiting subsurface spaces such as aquifers, porous rock formations, and caverns to store surplus thermal energy during periods of low demand and retrieve it when energy needs rise [2].

Aquifer thermal energy storage (ATES) is a widely implemented UTES technology that uses cyclic water injection and extraction to satisfy heating requirements [3]. During summer, warm water is injected into the warm well for storage, while cool water is simultaneously extracted from the cold well to maintain aquifer pressure balance and prevent thermal interference. In winter, the process is reversed: the warm well extracts heated water for use, and cold water is re-injected into the cold well [4]. This bidirectional design ensures the aquifer's thermal stratification and hydraulic balance, enabling ATES to efficiently address seasonal heating needs in a scalable and economically viable manner [5]. With thousands of installations in Europe, particularly in countries like the Netherlands and Belgium, ATES has

* Corresponding author at: Department of Geology, Ghent University, Krijgslaan 281, Ghent, B-9000, Belgium.
** Corresponding author.
E-mail addresses: le.zhang@ugent.be (L. Zhang), liuliyuan@ustb.edu.cn (L. Liu).

https://doi.org/10.1016/j.energy.2025.137096
Received 8 March 2025; Received in revised form 10 June 2025; Accepted 11 June 2025
Available online 27 June 2025

Nomenclature

Symbols

ρ_f	Fluid density [kg/m^3]
φ	Porosity (-)
χ_f	Fluid compressibility [1/Pa]
p	Fluid pressure [Pa]
t	Time [s]
$\mathbf{u}$	Fluid flux vector [m/s]
Q_f	External mass source/sink [kg/(m^{3}s)]
k	Permeability [m^2]
μ	Fluid viscosity [Pa s]
$\mathbf{g}$	Gravitational acceleration vector [m/s^2]
ρ_s	Solid phase density [kg/m^3]
C_s	Specific heat capacity of the solid [J/(kg K)]
C_f	Specific heat capacity of the fluid [J/(kg K)]
T	Temperature [K]
Q_T	Heat source [W/m^3]
$\mathbf{q}$	Heat flux vector [W/m^2]
λ_{eq}	Equivalent thermal conductivity [W/(m K)]
λ_s	Thermal conductivity of the solid [W/(m K)]
λ_f	Thermal conductivity of the fluid [W/(m K)]
$\boldsymbol{\sigma}$	Total stress tensor [Pa]
ρ	Density of the porous medium [kg/m^3]
$\boldsymbol{\sigma}'$	Effective stress tensor [Pa]
$\mathbf{I}$	Identity tensor (-)
$\mathbf{C}$	Elastic stiffness matrix (function of E and ν)
$\boldsymbol{\epsilon}$	Strain tensor (-)
$\boldsymbol{\epsilon_{th}}$	Thermal strain (-)
E	Young's modulus [Pa]
ν	Poisson's ratio (-)
α_T	Coefficient of thermal expansion [1/K]
T_{ref}	Reference temperature [K]
$\dot{m}$	Mass flow rate [kg/s]
C_p	Specific heat capacity [J/(kg K)]
$T_{extraction}$	Extraction temperature [K]
$T_{injection}$	Injection temperature [K]
ϕ	Slip tendency (mobilized friction angle) (°)
τ	Shear stress [MPa]

Acronyms

UTES	Underground Thermal Energy Storage
ATES	Aquifer Thermal Energy Storage
HT-ATES	High-Temperature Aquifer Thermal Energy Storage
THM	Thermo-Hydro-Mechanical
DGSA	Distance-Based Generalized Sensitivity Analysis
NSGA-II	Non-dominated Sorting Genetic Algorithm II
LHS	Latin Hypercube Sampling
XGBoost	eXtreme Gradient Boosting
TRE	Thermal Recovery Efficiency
AHP	Annual Heat Production
CDFs	Cumulative Distribution Functions
TPR	True Positive Rate
TNR	True Negative Rate

demonstrated its maturity and reliability as a sustainable energy storage technology [6]. High-temperature aquifer thermal energy storage (HT-ATES, typically above 50 °C) [7] broadens the application scope of ATES by enabling energy storage at higher temperatures and deeper subsurface conditions, as shown in Fig. 1. Unlike conventional ATES, which primarily serves residential heating, HT-ATES is designed for

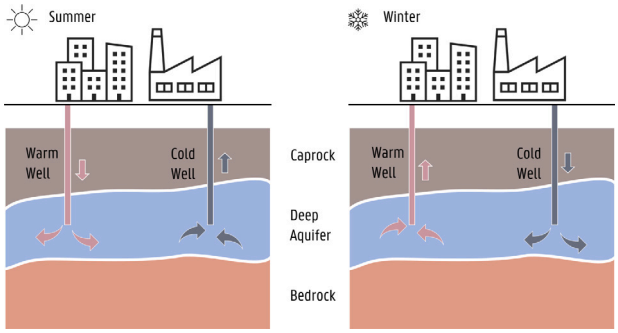

Fig. 1. Schematic of the high-temperature aquifer thermal energy storage (HT-ATES) system. The left panel shows heat storage through warm water injection and cold water extraction, while the right panel illustrates heat extraction with warm water production and cold water injection.

industrial-scale applications such as waste heat recovery, district heating, and large-scale seasonal energy storage [8]. Moreover, recent studies have explored the use of thermal storage for demand-side management, demonstrating overlapping benefits with HT-ATES in optimizing energy use and enhancing system flexibility [9].

HT-ATES technology is currently under active development, with notable pilot projects in Europe demonstrating mixed outcomes [10,11]. The Middenmeer project in the Netherlands supports one of the largest greenhouse complexes by utilizing a deep aquifer system for seasonal heat storage, showcasing its potential in industrial-scale applications [12]. Similarly, the TU Delft campus is piloting an integrated geothermal energy system that combines shallow thermal storage with deeper geothermal heat sources, aiming to enhance long-term efficiency [13]. However, some early initiatives faced significant challenges. For instance, the HT-ATES system at Utrecht University faced critical issues such as aquifer clogging and consistently low thermal recovery efficiency (TRE), leading to its abandonment [10]. A similar fate befell the system at Neubrandenburg, Germany, where pump corrosion and operational unreliability rendered the project unsustainable [12]. These projects highlight both the potential and challenges of HT-ATES, particularly the technical complexities of deep subsurface environments [14]. High temperatures, elevated pressures, and substantial geomechanical stresses intensify the coupling of thermo-hydro-mechanical (THM) processes, which are critical to system performance [15]. For example, high injection pressures can reduce effective stress in the reservoir, increasing the risk of caprock deformation or fault slippage. Elevated injection temperatures induce localized thermal expansion [16], creating stress gradients that destabilize interfaces, particularly between the reservoir and caprock [17]. Conversely, injecting cooler water into a high-temperature reservoir can cause thermal contraction, redistributing stresses and further compromising reservoir [18]. These dynamic interactions underscore the need for a comprehensive understanding of THM effects to predict reservoir behavior and implement effective risk mitigation strategies [19].

The challenges observed in HT-ATES projects highlight the necessity of detailed THM modeling and a comprehensive design strategy to system design [20]. Successful implementation of HT-ATES systems depends on identifying key parameters, accurately predicting system responses, and mitigating risks associated with complex THM couplings. Aquifer permeability strongly influences fluid flow and heat transfer, directly affecting the efficiency of thermal recovery [21]. Thermal stresses and porous elastic stresses are critical in mechanical stability, particularly in stress redistribution within the reservoir and caprock [22]. Design parameters such as well spacing and operational rate also impact both thermal performance and system stability by adjusting pressure gradients and stress concentrations [23]. These intricate dependencies highlight the complexity of parameter interactions in THM processes, marked by strong nonlinearities and couplings [24].

Addressing these challenges requires advanced methods capable of evaluating the influence of parameters across their full range while capturing intricate interdependencies. Distance-based generalized sensitivity analysis (DGSA) has been shown to excel in such contexts, with successful applications in multi-physics systems, including geothermal energy modeling and subsurface flow simulations [25]. By clustering output responses and analyzing their relationships with parameter distributions, DGSA identifies dominant parameters and quantifies their contributions to system behavior [26]. This approach not only enhances understanding of system dynamics but also provides a robust framework for optimizing performance and ensuring stability under complex operating conditions.

This study is the first effort to comprehensively assess both the thermal efficiency and geomechanical stability of HT-ATES systems by integrating coupled THM modeling, distance-based generalized sensitivity analysis (DGSA), and a surrogate-assisted multi-objective optimization framework using NSGA-II. A benchmark model is established to investigate the thermal and mechanical evolution of the system during operation, while DGSA quantifies key parameters' impacts and their coupled interactions. Subsequently, the surrogate-assisted NSGA-II optimization balances energy production and geomechanical safety, leading to optimal design solutions. The innovative framework, featuring a dual DGSA-driven variable screening approach integrated with a surrogate model, not only reduces computational costs but also enhances the robustness and physical fidelity of the optimized designs. The resulting Pareto front offers decision-makers valuable insights into the trade-offs between energy efficiency and operational safety, thus supporting the development of HT-ATES as a sustainable solution for large-scale energy storage.

2. Methodology

This study presents a comprehensive framework for HT-ATES systems by integrating coupled THM model, DGSA, and multi-objective optimization using the NSGA-II algorithm. The THM model simulates the forward behavior of the system, capturing its hydraulic, thermal, and mechanical responses, implemented in COMSOL Multiphysics. DGSA is employed to identify the dominant parameters and elucidate their interactions, providing valuable insights into heat recovery performance and reservoir stability under complex subsurface conditions. Finally, the NSGA-II algorithm is applied to optimize the design parameters, balancing energy efficiency and geomechanical safety, and yielding a set of Pareto-optimal solutions that effectively address the inherent trade-offs in HT-ATES operations. Fig. 2 provides a comprehensive overview of our methodological framework.

2.1. Governing equations

The coupled governing equations for the HT-ATES system include fluid mass balance, energy conservation, and mechanical equilibrium. Together, they describe the interactions between thermal, hydraulic, and mechanical processes in the subsurface.

The fluid mass balance equation captures the conservation of mass for the pore fluid, expressed as [27]:

$$\rho_{\mathrm{f}}\left(\varphi\chi_{\mathrm{f}}+\frac{\partial\varphi}{\partial p}\right)\frac{\partial p}{\partial t}+\nabla\cdot(\rho_{\mathrm{f}}\mathbf{u})=Q_f \tag{1}$$

where ρ_{f} is the fluid density, φ is the effective porosity, χ_{f} is the fluid compressibility, p is the fluid pressure, t is time, $\mathbf{u}$ is the fluid flux vector, and Q_{f} represents external mass sources or sinks. The fluid flux is governed by Darcy's law [27]:

$$\mathbf{u}=-\frac{k}{\mu}(\nabla p+\rho_{\mathrm{f}}\mathbf{g}) \tag{2}$$

where k is the permeability of the porous medium, μ is the fluid viscosity, and $\mathbf{g}$ is the gravitational acceleration vector.

Heat transport within the system is described by the energy conservation equation [27]:

$$\left[(1-\varphi)\rho_{\mathrm{s}}C_{\mathrm{s}}+\varphi\rho_{\mathrm{f}}C_{\mathrm{f}}\right]\frac{\partial T}{\partial t}+\rho_{\mathrm{f}}C_{\mathrm{f}}\mathbf{u}\cdot\nabla T+\nabla\cdot\mathbf{q}=Q_T \tag{3}$$

where ρ_{s} and C_{s} are the density and specific heat capacity of the solid phase, while ρ_{f} and C_{f} are the fluid phase's density and heat capacity, respectively. T is the temperature, Q_T is the heat source term, and $\mathbf{q}$ is the heat flux vector defined by Fourier's law [27]:

$$\mathbf{q}=-\lambda_{\mathrm{eq}}\nabla T \tag{4}$$

where λ_{eq} is the equivalent thermal conductivity, computed as [27]:

$$\lambda_{\mathrm{eq}}=(1-\varphi)\lambda_{\mathrm{s}}+\varphi\lambda_{\mathrm{f}} \tag{5}$$

where λ_{s} and λ_{f} are the thermal conductivities of the solid and fluid phases, respectively.

The mechanical equilibrium equation, based on the momentum balance principle, accounts for stress redistribution within the reservoir [27]:

$$\nabla\cdot\boldsymbol{\sigma}+\rho\mathbf{g}=\mathbf{0} \tag{6}$$

where $\boldsymbol{\sigma}$ is the total stress tensor and $\rho=\varphi\,\rho_f+(1-\varphi)\,\rho_s$ is the porous material's density, with φ the porosity, ρ_f the fluid density, and ρ_s the solid density. The effective stress $\boldsymbol{\sigma}'$ is related to the fluid pressure p by [27]:

$$\boldsymbol{\sigma}'=\boldsymbol{\sigma}-p\mathbf{I} \tag{7}$$

where $\mathbf{I}$ is the identity tensor. Assuming isotropic linear elasticity, the stress–strain relationship is expressed as [27]:

$$\boldsymbol{\sigma}=\mathbf{C}(\boldsymbol{\varepsilon}-\boldsymbol{\varepsilon}_{\mathrm{th}})+p\mathbf{I} \tag{8}$$

where $\mathbf{C}$ is the elastic stiffness matrix defined by Young's modulus E and Poisson's ratio ν. The thermal strain $\boldsymbol{\varepsilon}_{\mathrm{th}}$ is given by [27]:

$$\boldsymbol{\varepsilon}_{\mathrm{th}}=\alpha_T(T-T_{\mathrm{ref}})\mathbf{I} \tag{9}$$

where α_T is the coefficient of thermal expansion, and T_{ref} is the reference temperature.

Finally, temperature-dependent properties such as fluid viscosity μ, thermal conductivity λ_{f}, density ρ_{f}, and specific heat capacity C_{f} are incorporated into the model using empirical relations as described in [27].

The governing equations above are solved to simulate the coupled thermal, hydraulic, and mechanical responses of the HT-ATES system. The resulting pressure, temperature, and stress distributions serve as the basis for our DGSA, surrogate model construction, and multi-objective optimization, thereby integrating the physical model with the optimization process.

2.2. Model setup and parameter selection

Following common practice in THM coupling studies [19,28], we adopt a vertical 2D plane-strain model to capture the essential THM interactions while keeping computational cost manageable. The model spans a 400 × 400 m domain, with a 40 m thick reservoir positioned at its center. The depth of the reservoir's center is treated as a variable to simulate HT-ATES performance at different subsurface conditions. Similarly, the distance between the warm and cold wells within the reservoir is adjustable, allowing for the evaluation of varying well spacing on system performance. The well radius is fixed at 0.5 m.

The initial and boundary conditions are designed to replicate realistic subsurface environments. The temperature distribution within the model followed a geothermal gradient of 30 °C/km, starting from a surface temperature of 10 °C. Hydraulic pressure is assumed to follow a hydrostatic gradient, and the mechanical stress field incorporated the self-weight of the overburden rock. These gradients in temperature, hydraulic pressure, and stress-each varying with depth-defined the

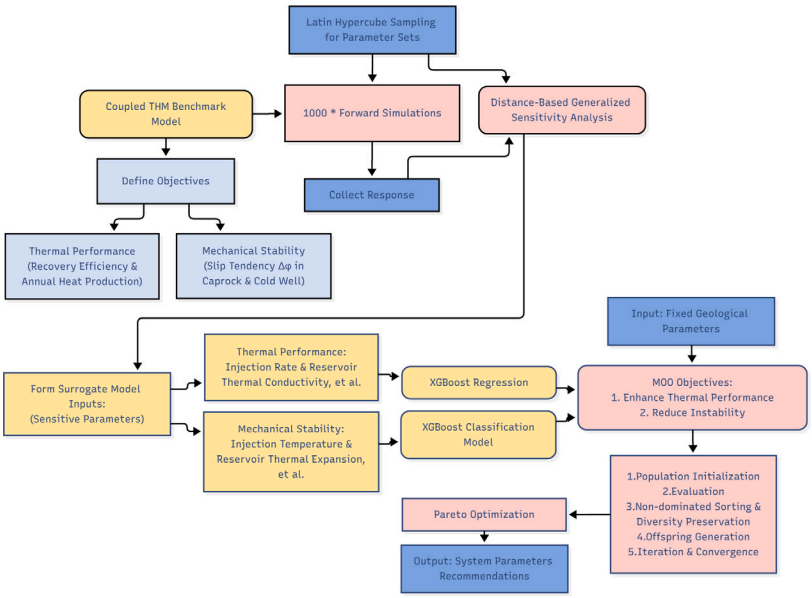

Fig. 2. Overview of the methodological framework for HT-ATES system optimization. The flowchart illustrates the process from forward THM simulation and Latin hypercube sampling for parameter sets, through distance-based generalized sensitivity analysis and surrogate modeling using XGBoost, to multi-objective optimization via NSGA-II.

Table 1
Parameter categories, benchmark values, sampling ranges, abbreviations, and symbols.

Parameter name [Unit]	Benchmark value	Sampling range	Abbreviation	Symbol
System Parameters				
Injection Rate [kg/s]	10	(5, 15)	Inj_rate	$\dot{m}$
Warm Well Injection Temperature [° C]	110	(40, 180)	T_w_inj	T_1
Cold Well Injection Temperature [° C]	20	(10, 30)	T_c_inj	T_2
Well Spacing [m]	150	(50, 250)	w_sp	–
Reservoir Depth [m]	800	(600, 1000)	Res_depth	–
Reservoir Properties				
Permeability (log) [m^2]	3×10^{-13}	(10^{-14}, 10^{-11})	Res_perm	k_{res}
Porosity [-]	0.20	(0.15, 0.25)	Res_poro	φ_{res}
Thermal Conductivity [W/(m K)]	2.0	(1.5, 2.5)	Res_cond	λ_{res}
Thermal Expansion (log) [1/K]	5×10^{-6}	(10^{-6}, 10^{-5})	Res_exp	α_{res}
Heat Capacity [J/(kg K)]	1150	(800, 1300)	Res_cp	C_{res}
Density [kg/m^3]	2150	(2000, 2300)	Res_rho	ρ_{res}
Young's modulus [GPa]	15	(10, 20)	Res_ym	E_{res}
Base Rock Properties				
Permeability (log) [m^2]	10^{-17}	(10^{-18}, 10^{-16})	Rock_perm	k_{rock}
Porosity [-]	0.015	(0.01, 0.025)	Rock_poro	φ_{rock}
Thermal Conductivity [W/(m K)]	3.0	(2.5, 3.5)	Rock_cond	λ_{rock}
Thermal Expansion (log) [1/K]	5×10^{-7}	(10^{-7}, 10^{-6})	Rock_exp	α_{rock}
Heat Capacity [J/(kg K)]	1500	(1000, 2000)	Rock_cp	C_{rock}
Density [kg/m^3]	2500	(2300, 2700)	Rock_rho	ρ_{rock}
Young's modulus [GPa]	15	(10, 20)	Rock_ym	E_{rock}

Note: The properties represent the solid phase. Subscripts "res" and "rock" distinguish reservoir and base rock properties, respectively.

initial conditions for the system. At the model boundaries, hydraulic heads and temperatures are fixed at the top and bottom, while lateral boundaries are set to be impermeable and adiabatic. Depth-dependent self-weight stress is applied at the top boundary, with roller supports along the sides, as illustrated in Fig. 3.

Throughout each year, the system alternates between rest, injection, rest, and extraction phases to mimic seasonal thermal storage. During the first quarter, both wells remain closed without any injection or extraction. In the second quarter, warm water at temperature T_1 is injected into the warm well at a controlled rate, while the cold well simultaneously extracts water at the same rate to maintain pressure balance. The system then enters another rest phase during the third quarter, followed by a final phase in which hot water is extracted from the warm well and cold water at temperature T_2 is injected into the cold well to sustain reservoir pressure. This operational cycle, illustrated in Fig. 4, represents the typical operational strategy for ATES systems [5]. Although in real scenarios the well cycling may be more complex and dynamic, this idealized case provides a robust basis for theoretical analysis and preliminary design. The cycle is repeated annually to evaluate long-term system performance over a 20-year simulation period [29], a base time step of 1/40 year is used throughout. Immediately after each boundary condition switch in each season, the time step is refined to 1/160 year for the first 1/5 of the season. For full details of the model verification, see Appendix A.

To evaluate the performance and stability of HT-ATES systems, a comprehensive set of parameters is considered to capture the variability in subsurface properties and operational conditions. These parameters are categorized into three groups: system setup, reservoir properties, and basic rock properties, as summarized in Table 1. Reservoir properties, including permeability, porosity, thermal conductivity, thermal expansion, heat capacity, density, and Young's modulus, govern fluid flow, heat transfer, and stress evolution within the storage reservoir, directly influencing thermal recovery and mechanical response. Similarly,

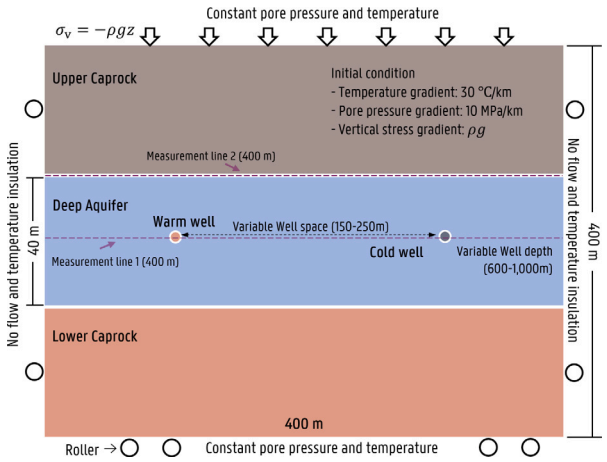

Fig. 3. Model setup for the HT-ATES system, showing the reservoir, caprock layers, well configuration, and initial and boundary conditions. Key analysis lines: measurement line 1 (400 m) - Horizontal line between the warm and cold wells; measurement line 2 (400 m) - Horizontal line along the caprock.

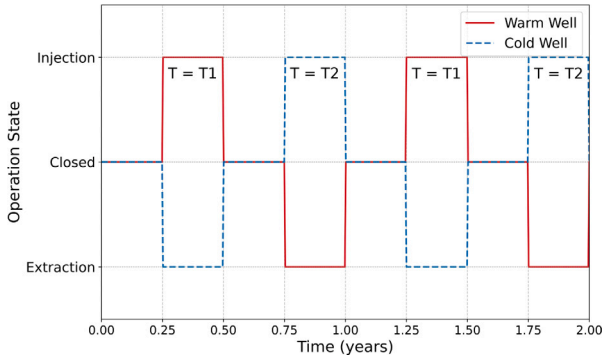

Fig. 4. Operational schedule for the HT-ATES system over a 20-year cycle (first two years shown). Each annual cycle consists of: (1) a quarter with both wells closed; (2) a quarter where the warm well injects water at temperature T_1 and the cold well extracts water at the same rate; (3) a quarter with both wells closed; and (4) a quarter where the warm well produces heat (extracting water) while the cold well is recharged at temperature T_2. The values of T_1 and T_2 are selected from the ranges given in Table 1.

basic rock properties characterize the surrounding geology, affecting boundary behavior and overall system stability. A benchmark parameter set is established to represent typical conditions and serves as a baseline for analyzing system responses, with detailed results provided in the following sections. To ensure a thorough exploration of the parameter space, latin hypercube sampling (LHS) is used to generate 1000 unique parameter sets within the specified ranges, enabling robust sensitivity analysis. In this study, we adopt a simplified 2D, linear elastic, and homogeneous model. This simplification enables us to run robust sensitivity analysis and surrogate-based multi-objective optimization with tractable computational cost. Our prior THM coupling analyses of heterogeneous geothermal systems have shown that heterogeneity has a limited effect on our key performance metrics, supporting the validity of the homogeneous approximation [24].

Furthermore, key performance metrics are defined as follows. TRE, which quantifies the fraction of injected heat recovered during operation, is defined by

$$TRE = \frac{\int_{t_1}^{t_2} \dot{m} C_p \left(T_{\text{extraction}} - T_{\text{ref}}\right) dt}{\int_{t_1}^{t_2} \dot{m} C_p \left(T_{\text{injection}} - T_{\text{ref}}\right) dt}, \tag{10}$$

where $\dot{m}$ is the mass flow rate, C_p is the specific heat capacity, $T_{\text{extraction}}$ and $T_{\text{injection}}$ are the extraction and injection temperatures, and T_{ref} is the reference temperature (typically the initial reservoir temperature).

In addition, annual heat production (AHP), which quantifies the total heat extracted over a specified period, is defined as

$$AHP = \int_{t_1}^{t_2} \dot{m} C_p \left(T_{\text{extraction}} - T_{\text{ref}}\right) dt. \tag{11}$$

Similarly, the mechanical response is evaluated using the slip tendency ϕ, defined as [24]:

$$\phi = \arctan\left(\frac{\tau}{\sigma'}\right), \tag{12}$$

where τ is the shear stress and σ' is the effective normal stress. A higher ϕ indicates a region closer to shear failure and hence a higher risk of instability.

These definitions establish the theoretical foundation for assessing both thermal and mechanical performance, and they are integrated with the forward simulation outputs to support the subsequent sensitivity analysis and optimization process.

2.3. Distance-based Generalized Sensitivity Analysis

Distance-based Generalized Sensitivity Analysis (DGSA) classifies complex outputs into clusters and then quantifies parameter sensitivities based on cluster-wise distribution differences [26]. In our implementation, we first apply a distance-based clustering algorithm (K-medoids with Euclidean distance) to group the stochastic simulation results. Specifically, the time series of thermal performance and slip tendency from each realization are used as clustering features. We set the number of clusters to three, as this choice yields clearly distinguishable groups while maintaining roughly balanced sample sizes in each cluster. For each cluster, the cumulative distribution function (CDF) of each input parameter is compared against the overall CDF; sensitivity indices are computed from the normalized L1-distance between these distributions. Parameters whose sensitivity values exceed a predefined threshold (set to 1 in this study) are deemed important. DGSA also supports the computation of second-order (conditional) sensitivities, which capture the interactions between parameter pairs. For more details, see Appendix B.

DGSA is particularly well suited for HT-ATES applications because it can directly handle high-dimensional, time-dependent, and spatio-temporal outputs without requiring any a priori dimensionality reduction [30]. It also accommodates different input types (both continuous and discrete) within a single framework. Moreover, DGSA requires relatively few model runs because its computational cost is far lower than that of full-model Sobol evaluations [31], making it feasible for coupled thermo-hydro-mechanical simulations. Finally, the output clusters and associated parameter distributions produced by DGSA are easy to visualize and interpret, revealing which factors drive distinct response patterns.

2.4. Optimization framework

The primary objective of this study is to determine an optimal set of design parameters for HT-ATES systems, balancing the maximization of energy performance with the minimization of system damage risk. Given that the geological (formation) parameters are fixed for a given site, the optimization focuses exclusively on system parameters. The multi-objective optimization problem is formulated to simultaneously maximize heat performance (f_1) and minimize geomechanical failure risk (f_2):

$$\max_{\mathbf{x}} \quad f_1(\mathbf{x};\mathbf{y}) \quad \text{(thermal performance metrics, e.g., TRE [Eq. (10)] and AHP [Eq. (11)])},$$
$$\min_{\mathbf{x}} \quad f_2(\mathbf{x};\mathbf{y}) \quad \text{(slip tendency, as defined in Eq. (12))}.$$

where $\mathbf{x}$ represents the set of controllable design parameters (e.g., injection rate, well temperatures, well spacing) and $\mathbf{y}$ denotes fixed geological properties. Note that each objective function may depend

on a different subset of the design parameters; details of the parameter selection and their optimization ranges are provided in Section 3.3.1 and summarized in Table 1. We establish a three-stage optimization workflow:

1. **Parameter Screening**: We apply DGSA separately for each objective function to identify the dominant parameters. For f_1, we identify a subset $\mathbf{x}_{s1} \subseteq \mathbf{x}$ and $\mathbf{y}_{s1} \subseteq \mathbf{y}$ that predominantly influences f_1; for f_2, we identify a potentially different subset $\mathbf{x}_{s2} \subseteq \mathbf{x}$ and $\mathbf{y}_{s2} \subseteq \mathbf{y}$ that has the greatest impact on f_2. This differentiated variable screening reduces the dimensionality of each surrogate model's input space and ensures that the models capture the core physical dynamics relevant to each objective.
2. **Surrogate Modeling**: We develop two types of surrogate models-one for each objective. For f_1 (which predicts key performance metrics such as TRE and AHP), we build eXtreme Gradient Boosting (XGBoost) regression models; for f_2 (geomechanical failure risk), we develop XGBoost classification models. XGBoost is chosen for its robustness, ability to capture complex non-linear interactions, and effective regularization [32]. Prior to model training, we preprocess the simulation data by first selecting sensitive parameters via DGSA, thereby reducing the input feature set to $\mathbf{x}_{s1}$ and $\mathbf{y}_{s1}$ for f_1 and $\mathbf{x}_{s2}$ and $\mathbf{y}_{s2}$ for f_2. The data are then split into training and validation sets, and input features are standardized to ensure consistency; necessary inverse transformations are applied to restore the surrogate outputs to their original physical scales. During training, hyperparameter tuning is performed using cross-validation, optimizing evaluation metrics such as R^2 and RMSE for the regression models, and classification accuracy (supported by confusion matrix analysis) for the classifiers. Cross-validation ensures that our surrogate models can reliably predict high-fidelity simulation outputs, enabling their efficient integration with the NSGA-II optimization algorithm.
3. **Multi-Objective Optimization**: We employ the NSGA-II algorithm [33] as our evolutionary optimization method. This algorithm uses selection, crossover, and mutation to identify a Pareto front, which is a set of non-dominated solutions representing optimal trade-offs among conflicting objectives. The algorithm proceeds through the following steps:

    - **Population Initialization**: Generate an initial population (e.g., 100 individuals) by randomly sampling from the design space defined by the engineering constraints, where each candidate represents a set of controllable parameters.
    - **Evaluation**: Evaluate each candidate using surrogate models for f_1 (heat performance) and f_2 (geomechanical risk), efficiently approximating the objectives without relying on gradient-based methods.
    - **Non-dominated Sorting and Diversity Preservation**: Rank candidates using Pareto dominance via non-dominated sorting, and compute crowding distances-which measure the density of solutions in the objective space-to promote diversity by favoring solutions in less crowded regions.
    - **Offspring Generation**: Generate offspring using genetic operators:
        - **Tournament Selection**: Choose parent candidates based on Pareto rank and crowding distance.
        - **Simulated Binary Crossover**: Combine parent solutions to create new candidates for continuous variables.
        - **Polynomial Mutation**: Introduce small random perturbations to maintain diversity and avoid local optima.
    - **Iteration and Convergence**: Merge offspring with the existing population and iterate until the Pareto front stabilizes, indicating negligible further improvements in the trade-offs.

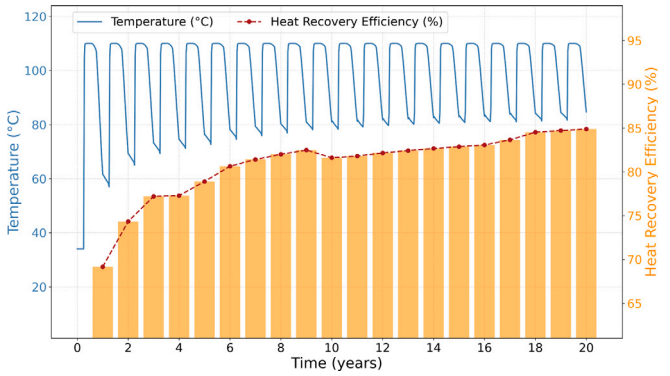

Fig. 5. Temporal evolution of warm well temperature (° C, left axis) (note: "production temperature" refers to the warm well temperature during the last quarter of each year; at all other times the warm well is not in production) and heat recovery efficiency (%, right axis) over 20 years of HT-ATES operation.

The innovative aspect of the proposed framework lies in its dual DGSA-driven variable screening approach and its integration with a surrogate-assisted NSGA-II optimization strategy. Specifically, the dual DGSA method first identifies distinct sets of sensitive parameters for each objective by analyzing their individual influence on the system's performance. This is followed by a comprehensive evaluation of parameter interactions, which helps in refining the variable screening process. In parallel, a surrogate model is constructed to approximate the objective functions, allowing for a significant reduction in computational costs during the optimization process. The integration of this surrogate-assisted NSGA-II strategy not only accelerates the convergence of the algorithm but also enhances the robustness and physical fidelity of the optimized designs. The final Pareto front generated by the framework provides a set of optimal trade-off solutions, offering decision-makers deeper insights into the balance between energy production and operational safety.

3. Results

3.1. Benchmark model evaluation

The benchmark model is used to evaluate the long-term performance and stability of the HT-ATES system under typical subsurface and operational conditions. In this evaluation, we focus on two key aspects: the thermal performance (observed in the warm well) and the mechanical stability (particularly in regions prone to instability such as the caprock and cold well).

3.1.1. Thermal performance assessment

Fig. 5 shows the evolution of warm well temperature (blue curve) and TRE (orange curve) over 20 years, TRE is calculated solely for the warm well, as the cold well primarily ensures hydraulic stability and thermal interference mitigation. Initially, production temperature exhibits large cyclic fluctuations (approximately 55 °C in year 1). Over time, the amplitude reduces-down to 30 °C by year 7 and stabilizing around 25 °C-indicating improved thermal stability as the system approaches equilibrium. Similarly, TRE starts at about 70% due to high heat losses and increases steadily, surpassing 80% by year 6 and stabilizing at approximately 85% by year 18.

Overall, these results demonstrate that under typical subsurface conditions, the HT-ATES system can achieve high TRE and enhanced thermal stability, providing a robust basis for further optimization.

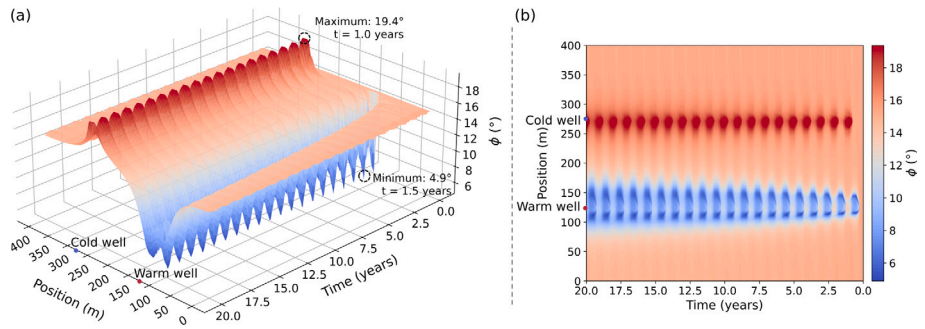

Fig. 6. Temporal variation of slip tendency ϕ (°) along measurement line 1, spanning the cold well region, during 20 years of operation: (a) 3D view; (b) 2D projected heat map.

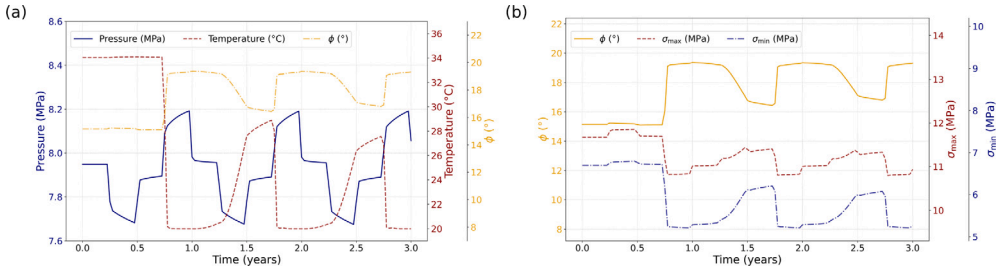

Fig. 7. Temporal evolution of pressure (MPa), temperature (°C), slip tendency ϕ (°), maximum principal stress σ_{max}, and minimum principal stress σ_{min} near the cold well over the first three years of operation.

3.1.2. *Mechanical response at the cold well*

Fig. 6 shows the temporal evolution of ϕ along line 1 (see Fig. 3) over 20 years. The cold well shows a peak ϕ of 19.4° at the end of the first operational year, indicative of a higher instability risk due to cooling-induced contraction and pressure increases. In contrast, the warm well exhibits a more stable response with a minimum ϕ of 4.9° at around 1.5 years, where the stabilizing effect of thermal expansion outweighs the destabilizing influence of increased pore pressure.

Figs. 7 provide detailed evolution of pressure (p), temperature (T), and ϕ -along with the maximum and minimum principal stresses (σ_{max} and σ_{min})- in the cold well region during the first three years. Taking the period from 1 to 2 years as an example, the cyclic response is divided into four distinct phases:

1. **Cold Well Closed Phase (1.0–1.25 years):**
   After a cold water injection, the cold well is closed. During this phase, p, T, and ϕ exhibit minor variations as the system remains quasi-stable. Temperature increases slowly due to heat conduction from the surrounding rock, and the principal stresses remain nearly constant, resulting in a stable ϕ.
2. **Cold Well Extraction Phase (1.25–1.5 years):**
   In the extraction phase, fluid removal causes a sharp drop in p and a transient rise in both σ_{max} and σ_{min}. Concurrently, T begins to recover more rapidly. The ensuing thermal expansion is constrained by the surrounding formation, converting into additional compressive stress. This process gradually reduces ϕ, indicating improved stability.
3. **Cold Well Closed Phase (1.5–1.75 years):**
   With extraction ceased, the well is closed again. Here, p recovers slightly while T continues its slow increase, leading to minor further reductions in ϕ as long-term thermal stresses stabilize the region.
4. **Cold Well Injection Phase (1.75–2.0 years):**
   During the subsequent injection phase, reintroduction of cold water causes p to rise rapidly and T to drop sharply. The swift decrease in T and associated rapid drop in principal stresses produce a sharp increase in ϕ. As the cold water zone expands and fluid viscosity increases, p begins to rise gradually, with the deterioration in mechanical stability slowing, though ϕ continues to increase overall.

Over successive cycles, the amplitude of fluctuations in p, T, and ϕ diminishes as the system gradually approaches a quasi-steady state under cyclic loading. Nevertheless, the consistently higher ϕ values during injection phases underscore the inherent vulnerability of the cold well to mechanical instability, indicating that the first year is critical for absolute stability. It is important to note that in practical applications, wells are typically screened over a finite thickness rather than modeled as point injections. Consequently, chemical reaction-induced clogging could result in localized pressure build-up within the screened interval, further exacerbating the instability observed in the cold well. Overall, while the warm well benefits from the stabilizing effects of thermal expansion-even in the presence of elevated pore pressure-the cold well is predominantly destabilized by the combined effects of cooling and pressure changes.

3.1.3. *Mechanical response at the caprock*

Figs. 8 and 9 illustrate the evolution of displacement and the slip tendency (ϕ) along line 2 (caprock section) over the simulation period, highlighting contrasting responses above the warm and cold wells. In the region above the warm well, displacement increases continuously-reaching a maximum of 5.9 mm by year 19.5-due to cumulative thermal expansion driven by sustained high-temperature injection. In contrast, displacement above the cold well remains low, with minor negative values in early years due to local thermal contraction.

The slip tendency ϕ above the warm well exhibits periodic fluctuations, with a peak of 34° around year 8.5. This peak reflects the delayed transmission of reservoir thermal expansion effects to the caprock. In the early years, the reservoir's thermal expansion primarily affects its internal volume, with minimal stress transfer to the caprock. As temperature accumulates, induced thermal stresses significantly increase the shear stress on the caprock, resulting in a rise in ϕ. Notably, while displacement accumulates gradually, ϕ offers an immediate indicator of mechanical stability.

Figs. 10 provide further details on the evolution of pressure (p), temperature (T), and ϕ -along with maximum and minimum principal

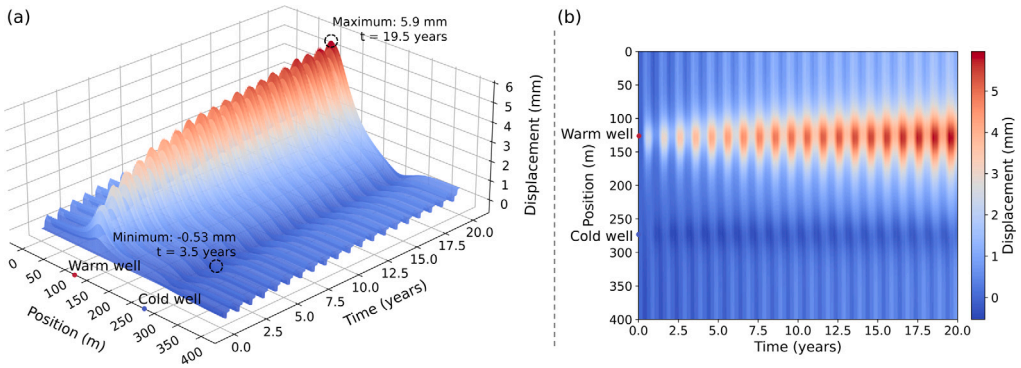

Fig. 8. Temporal variation of displacement (mm) along measurement line 2, spanning the cold well region, during 20 years of operation: (a) 3D view; (b) 2D projected heat map.

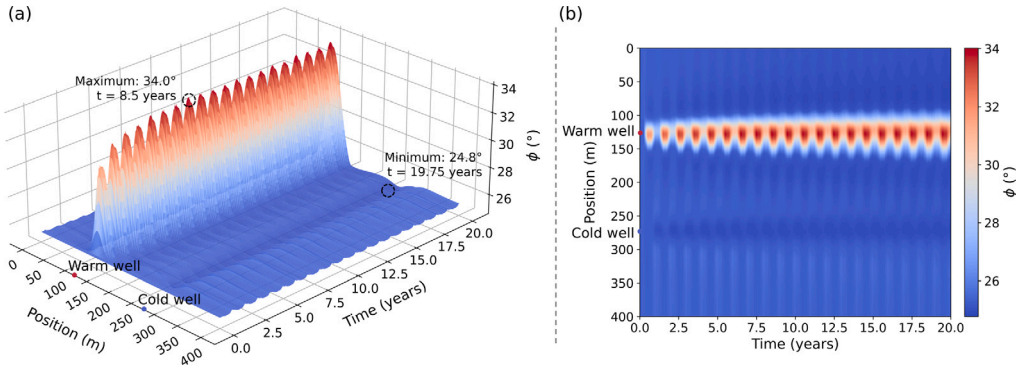

Fig. 9. Temporal variation of slip tendency ϕ (°) along measurement line 2, spanning the cold well region, during 20 years of operation: (a) 3D view; (b) 2D projected heat map.

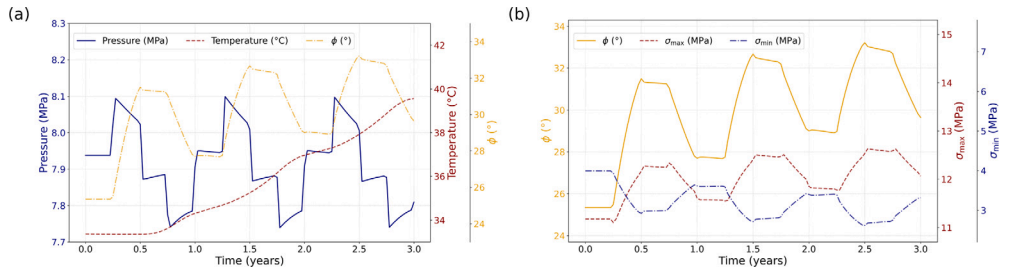

Fig. 10. Temporal evolution of pressure (MPa), temperature (°C), slip tendency ϕ (°), maximum principal stress σ_{max}, and minimum principal stress σ_{min} near the caprock above the warm well over the first three years of operation.

stresses (σ_{max} and σ_{min})- near the caprock above the warm well during the first three years. Taking the period from 1 to 2 years as an example:

- **Warm Well Closed Phase (1–1.25 years):**
  The caprock temperature increases slowly while remaining near the warm well. During this period, ϕ shows little variation.
- **Warm Well Injection Phase (1.25–1.5 years):**
  As hot water injection commences, p experiences a rapid rise, while T continues to increase steadily. The rapid increase in p causes a short-term slight decrease in the principal stresses (σ_{max} and σ_{min}). However, as the reservoir heats up further, thermal expansion is constrained by the surrounding rock, converting into additional compressive stress. This results in a gradual increase in σ_{max} (vertical stress) and a decrease in σ_{min} (horizontal stress), leading to an increase in ϕ from 27.8° to 33°, signaling a critical loss of stability.
- **Warm Well Closed Phase (1.5–1.75 years):**
  Following the cessation of injection, a rapid drop in p produces a small reduction in ϕ.
- **Warm Well Extraction Phase (1.75–2 years):**
  During the extraction phase, the long-term effect of thermal stress becomes dominant. As the reservoir cools slightly, the vertical compressive stress is reduced and the horizontal tensile stress recovers, resulting in a further decrease in ϕ and improved caprock stability.

Overall, each operational cycle results in a slight cumulative increase in σ_{max} and a decrease in σ_{min}, leading to an overall gradual increase in ϕ. This cumulative effect, driven by repeated thermal expansion and contraction of the reservoir, explains why the maximum ϕ in the caprock is observed at year 8.5.

In summary, while cumulative displacement reflects long-term deformation due to thermal expansion, the slip tendency ϕ responds more immediately to changes in thermal and mechanical conditions, making it a more sensitive indicator for assessing caprock stability. These findings underscore the critical role of reservoir-induced thermal stresses and suggest that the elevated ϕ values may be associated with an increased risk of induced seismicity or caprock shearing/fracturing, depending on the caprock's mechanical properties. Monitoring long-term temperature evolution and stress transmission in HT-ATES systems

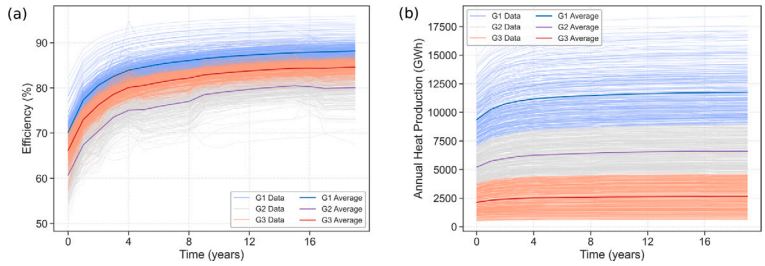

Fig. 11. Time evolution of (a) TRE and (b) AHP over 20 years of system operation. The simulation results are classified into three groups (G1, G2, and G3) based on clustering analysis, with the solid lines representing the mean trend of each group.

is therefore essential for early detection of potential failure and for designing mitigation strategies.

3.2. Sensitivity analysis

A comprehensive understanding of the key factors affecting the performance and stability of HT-ATES systems is essential for optimal design and efficient operation. In this study, we employ DGSA to assess the influence of critical operational and geological parameters on system behavior. The analysis is performed across three primary aspects:

1. **Thermal Performance**, quantified by thermal recovery efficiency (TRE) and annual heat production (AHP).
2. **Cold Well Stability**, evaluated through the change in slip tendency ($\Delta\phi$) from its initial value.
3. **Caprock Stability**, also assessed via $\Delta\phi$ in the caprock above the warm well.

Simulation outcomes are clustered into three groups (G1, G2, and G3) based on system response patterns. These clusters represent distinct response trends rather than inherently superior or inferior performance. The following subsections discuss the sensitivity analysis results for three primary aspects.

3.2.1. Thermal performance sensitivity

Fig. 11 shows the time evolution of (a) TRE and (b) AHP over 20 years. Initially, TRE exhibits significant variation among clusters; however, as the reservoir gradually warms over the first 5 years, the temperature gradient between the injected fluid and the formations diminishes, thereby reducing conductive heat loss. This results in a more efficient retention of thermal energy, which is reflected in the stabilized TRE values by year 20-approximately 88% for G1, 85% for G2, and between 75% and 80% for G3. In parallel, the cumulative warming enhances the overall thermal storage capacity of the reservoir, leading to an upward trend in AHP. By the 20th year, G1 cases achieve production levels around 12,000 GWh, while G3 cases are closer to 2500 GWh. Thus, the progressive increase in reservoir temperature underpins both the improved heat recovery and the enhanced energy output.

As shown in Figs. 12 (a1) and 13 (a1–e1), the injection rate is identified as the most critical parameter affecting TRE. A higher injection rate delivers a larger volume of heated water into the reservoir over a given period, thereby rapidly diminishing the relative impact of heat losses through conduction and convection. In addition, reservoir properties play a pivotal role in confining thermal energy. Specifically, a lower thermal conductivity minimizes heat diffusion into adjacent formations, while reduced permeability limits convective mixing between the injected hot water and native fluids, promoting a stable thermal stratification that enhances energy retention. Furthermore, a higher heat capacity enables the reservoir to store more thermal energy with minimal temperature fluctuations. Importantly, a lower thermal expansion coefficient is advantageous because excessive expansion can enhance convective heat transfer, causing heat to be transferred more rapidly to the caprock or surrounding formations rather than being effectively stored. Together, these factors highlight that both operational parameters and intrinsic reservoir properties are essential for optimizing TRE in HT-ATES systems. In contrast, Fig. 12 (a2) and Fig. 13 (a2–e2) highlight that injection temperature and injection rate are the dominant parameters for AHP. Higher injection temperatures directly increase the total thermal energy stored, leading to greater heat extraction. Likewise, increasing the injection rate boosts heat production by introducing more hot water per unit time, thereby improving thermal performance. It should be noted, however, that while a higher injection rate benefits thermal performance, it may also lead to increased injection pressure, which could potentially influence system stability.

Further analysis of parameter interactions reveals distinct effects for TRE and AHP. For TRE, as shown in Fig. 12 (b1), there is a strong dependency between injection rate and reservoir permeability. In low-permeability reservoirs, increasing the injection rate significantly enhances TRE by minimizing conductive and convective heat losses, thereby improving energy retention. In high-permeability systems, however, the benefit of a higher injection rate is less pronounced due to enhanced convective mixing and greater thermal dispersion. Moreover, the interaction between injection rate and reservoir heat capacity is notable. A higher heat capacity allows the reservoir to absorb more thermal energy and buffer temperature fluctuations, reinforcing the positive impact of an increased injection rate on TRE. Conversely, a lower heat capacity leads to steeper temperature gradients and faster heat loss, which limits the efficiency of heat recovery. In contrast, for AHP, as depicted in Fig. 12 (b2), the relationship between injection rate and injection temperature is critical. Higher injection temperatures not only increase the total thermal energy available for storage but also amplify the positive effects of an increased injection rate, resulting in greater heat storage and higher annual energy output. Thus, while both TRE and AHP benefit from a high injection rate, TRE is more sensitive to reservoir physical properties, whereas AHP is largely governed by the synergistic effects of injection rate and injection temperature.

3.2.2. Cold well stability sensitivity

To quantify stability, we adopt the change in slip tendency, $\Delta\phi$, as an indicator. This approach is motivated by two considerations. First, using $\Delta\phi$ helps mitigate the influence of sample-to-sample variations in the initial slip tendency, enabling a more consistent comparison across different scenarios. Second, rather than directly classifying a system as stable or unstable based on an absolute threshold, $\Delta\phi$ provides a quantitative measure of the system's deviation from its initial state. A larger $\Delta\phi$ suggests that the system may be more susceptible to failure. Note that while this metric effectively captures relative changes, its interpretation should account for the initial value of ϕ, as a small change may still be critical if the initial value is high.

The temporal evolution of $\Delta\phi$ at the cold well is presented in Fig. 14. Overall, the variations in $\Delta\phi$ differ markedly among the groups. In group G3, $\Delta\phi$ values exceed 10°, suggesting a potentially hazardous state. In contrast, both G1 and G2 exhibit minimal variations, with

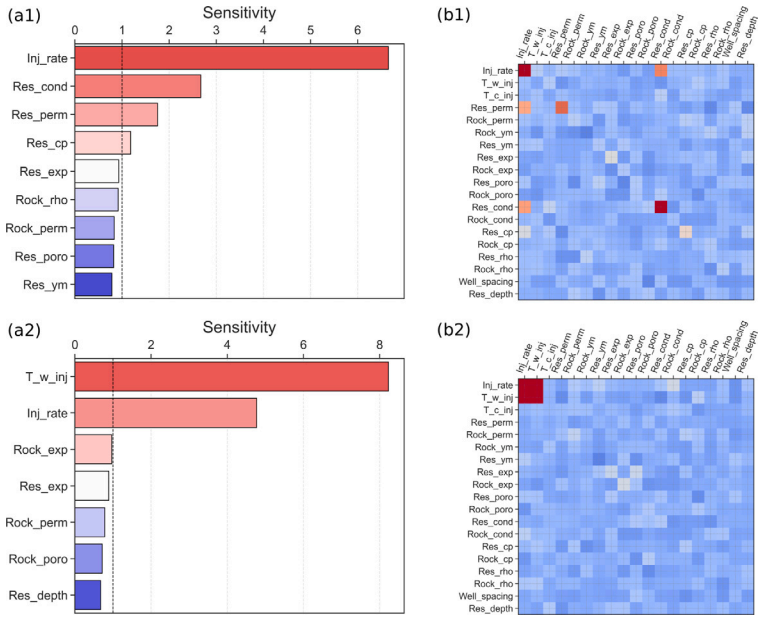

Fig. 12. Sensitivity analysis of (a1) TRE and (a2) AHP. The bar charts indicate the relative importance of key parameters, while (b1) and (b2) illustrate the interaction effects between parameters, with darker colors signifying stronger interactions.

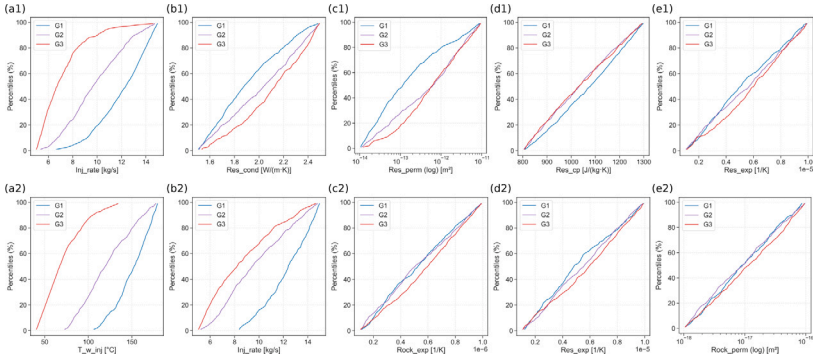

Fig. 13. Cumulative distribution functions (CDFs) of the top five most influential parameters for (a1–e1) TRE and (a2–e2) AHP. Each subplot compares the distribution of the parameter within the three groups (G1, G2, and G3).

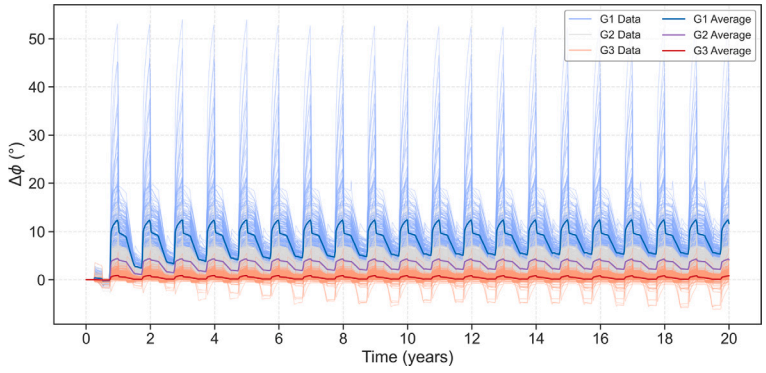

Fig. 14. Time evolution of cold well stability over 20 years of system operation. The simulation results are classified into three groups (G1, G2, and G3) based on clustering analysis, with the solid lines representing the mean trend of each group.

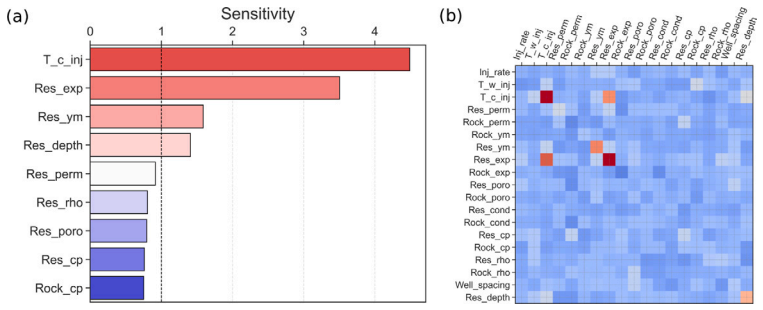

Fig. 15. Sensitivity analysis of (a) cold well stability. The bar charts indicate the relative importance of key parameters, while (b) illustrate the interaction effects between parameters, with darker colors signifying stronger interactions.

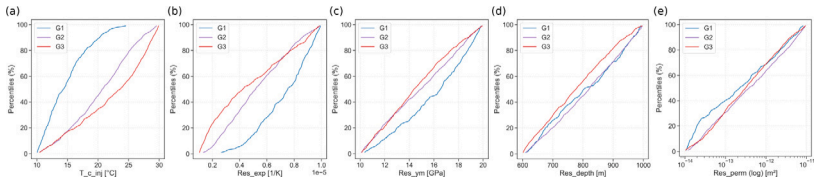

Fig. 16. Cumulative distribution functions (CDFs) of the top five most influential parameters for cold well stability. Each subplot compares the CDFs for three clusters (G1, G2, and G3) as determined by the clustering analysis in Fig. 14. The horizontal separation of the CDF curves directly reflects parameter sensitivity; larger separations indicate higher sensitivity.

some samples in G1 even showing negative $\Delta\phi$, indicating an enhancement in stability. The periodic fluctuations in $\Delta\phi$ clearly reflect the cyclic operation of the thermal reservoir system, where the annual injection and extraction processes induce systematic variations in the local stress state.

The sensitivity analysis results for cold well stability is provided in Fig. 15(a) and further detailed in Fig. 16, higher injection temperatures enhance system safety by reducing the thermal gradient between the injected fluid and the reservoir, which minimizes thermal stresses and results in a lower $\Delta\phi$. In contrast, the reservoir's thermal expansion coefficient now exhibits an opposite trend: a larger α leads to greater thermal strains, and by Hooke's law and the thermal stress relation, this translates into higher thermal stresses that directly increase $\Delta\phi$, thereby elevating the risk of failure. The third most sensitive parameter is the reservoir's Young's modulus; higher values of E amplify the conversion of thermal strain into thermal stress, further increasing $\Delta\phi$. Reservoir depth also plays a role, shallower reservoirs are found to be safer since their reservoir temperatures are lower, which reduces the temperature difference with the injected cold water and lessens induced thermal stresses. Finally, lower reservoir permeability is associated with higher $\Delta\phi$, possibly due to an enhanced impact of poroelastic stresses and the formation of localized low-temperature zones that steepen temperature gradients.

The interaction sensitivity analysis, presented in Fig. 15(b), reveals that the most significant coupled effect is between the injection temperature and the reservoir's thermal expansion coefficient. Specifically, lower injection temperatures combined with higher thermal expansion coefficients lead to substantially increased thermal stresses and, consequently, larger $\Delta\phi$, underscoring the dominant role of thermal stress in influencing system stability.

In summary, injection temperature and reservoir thermal expansion coefficient are the primary factors affecting $\Delta\phi$, with additional contributions from Young's modulus, permeability, and reservoir depth. These results highlight the importance of accounting for both individual parameter effects and their interactions in evaluating thermal reservoir stability.

3.2.3. Caprock stability sensitivity

The temporal evolution of $\Delta\phi$ for the caprock is shown in Fig. 17, where pronounced periodic fluctuations mirror the cyclic operation of the thermal reservoir system. Annual injection and extraction cycles induce alternating thermal stresses, leading to recurring variations in caprock stability. Notably, Group G1 exhibits large variations with mean peaks around 20°, Group G2 shows moderate peaks near 10°, and Group G3 remains relatively stable. Overall, these trends suggest that the caprock is inherently more vulnerable than the cold well. Likely due to the direct compression imposed on the caprock by the reservoir's vertical expansion, which elevates shear stress and creates a "sandwich-like" stress concentration structure-characterized by a rigid upper layer overlying the thermally expanding reservoir. It is noteworthy that within Group G1, a subset of extreme samples exhibits a rapid and pronounced increase in $\Delta\phi$ during the first year. These cases are associated with injection rates exceeding 10 kg/s and reservoir permeability lower than 2×10^{-14} m^2. Under these conditions, the high injection rate leads to a sharp pressure build-up during injection, resulting in a swift decrease in effective stress and a rapid rise in $\Delta\phi$. Although increased injection rates generally enhance thermal performance, this finding illustrates a critical trade-off: the potential for excessive pressure may undermine stability. Interestingly, while these extreme cases display very high $\Delta\phi$ values initially, the trend reverses in subsequent years. As the temperature in the warm well region gradually increases, the dynamic viscosity of the fluid decreases, which in turn reduces the pressure gradient and overall pressure. Consequently, the poroelastic stresses affecting the caprock are slightly alleviated over time.

The sensitivity analysis for caprock stability is presented in Fig. 18(a) and further detailed in Fig. 19. Injection temperature emerges as the most critical parameter, exhibiting the highest sensitivity. Higher injection temperatures, within the range of 40–180 °C, produce larger temperature differentials (ΔT), which lead to significant increases in vertical stress and, consequently, shear stress. In essence, larger ΔT results in higher $\Delta\phi$ in the caprock. Closely following is the reservoir's thermal expansion coefficient, α, which exhibits high sensitivity. A larger α leads to increased vertical strain within the reservoir, thereby intensifying the vertical compressive loading imposed on the overlying caprock. This enhanced vertical stress transfer can compromise caprock stability by amplifying the induced thermal stresses. Other parameters, such as reservoir depth and the properties of the basement rock, also exert moderate influences on caprock integrity. For instance, shallower reservoirs and caprocks with lower density are more detrimental because such conditions result in lower initial in-situ stresses, which

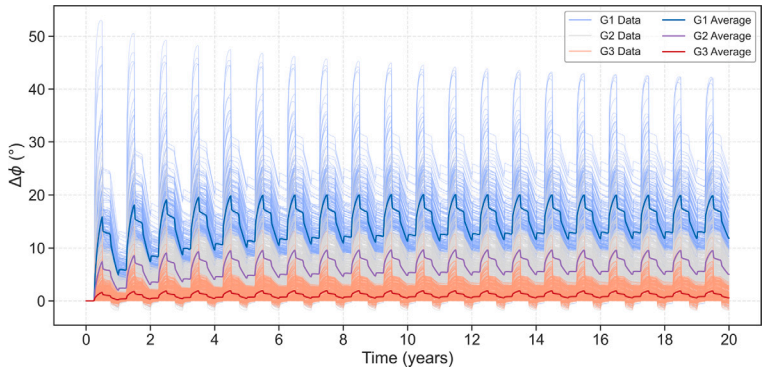

Fig. 17. Time evolution of caprock stability over 20 years of system operation. The simulation results are classified into three groups (G1, G2, and G3) based on clustering analysis, with the solid lines representing the mean trend of each group.

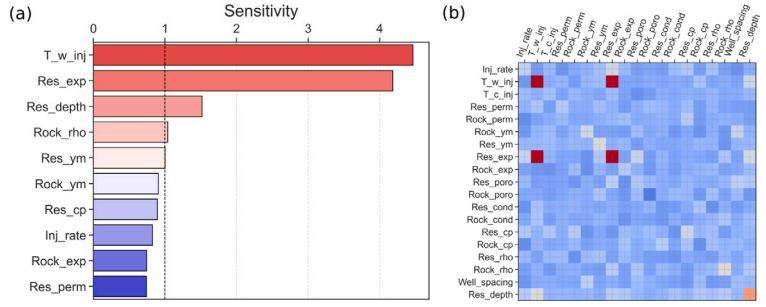

Fig. 18. Sensitivity analysis of (a) caprock stability. The bar charts indicate the relative importance of key parameters, while (b) illustrate the interaction effects between parameters, with darker colors signifying stronger interactions.

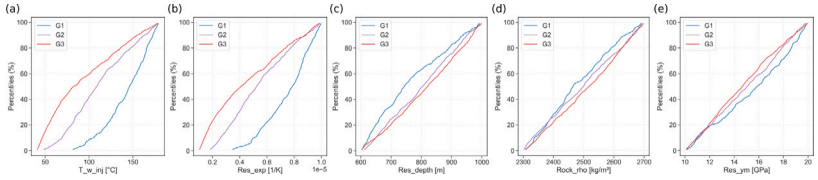

Fig. 19. Cumulative distribution functions (CDFs) of the top five most influential parameters for caprock stability. Each subplot compares the CDFs for three clusters (G1, G2, and G3) as determined by the clustering analysis in Fig. 17. The degree of horizontal separation among the CDF curves directly reflects the sensitivity of each parameter, with greater separation indicating higher sensitivity.

provide less restraint on reservoir expansion and allow for a greater vertical stress to be transmitted to the caprock. Moreover, shallower reservoirs generally exhibit lower initial temperatures, leading to a larger temperature differential with the injected hot water, while a higher Young's modulus in the reservoir material further exacerbates the stress transfer.

Parameter interaction analysis (see Fig. 18(b)) reveals that the combined effect of injection temperature and the reservoir's thermal expansion coefficient is particularly significant, as their product directly amplifies vertical stress. Moreover, our analysis indicates a trade-off: while higher injection temperatures enhance thermal efficiency by increasing the total stored thermal energy, they also elevate vertical stresses, thereby potentially compromising system stability.

In summary, our analysis reveals that the caprock above the warm well is subjected to significant stability challenges. Elevated injection temperatures and high thermal expansion properties induce substantial vertical stress buildup, which is transmitted to the caprock as vertical compression. This compression, in turn, increases the shear stress, ultimately leading to conditions conducive to caprock failure. These findings highlight the critical need for careful management of injection parameters and a comprehensive consideration of thermal and mechanical interactions in ensuring the long-term stability of thermal reservoir systems.

3.3. Optimization and surrogate model validation

3.3.1. Surrogate model development and performance evaluation

Based on the DGSA results, the injection rate, warm well injection temperature, and cold well injection temperature are identified as the most sensitive operational parameters. Accordingly, our optimization strategy focuses on these three design variables, denoted by the vector $\mathbf{x}$. For a given site, the geological properties are predetermined and remain fixed; these are denoted by $\mathbf{y}$. Thus, the optimization is performed solely over the operational parameters, while the geological parameters are treated as fixed inputs.

The optimization objectives are defined as follows, aiming to enhance energy production f_{1-1} and f_{1-2} while simultaneously reducing geomechanical risk f_{2-1} and f_{2-2}:

1. Maximize TRE, $f_{1-1}(\mathbf{x_{s1-1}}; \mathbf{y_{s1-1}})$, evaluated from the system's performance in the 20th year.
2. Maximize AHP, $f_{1-2}(\mathbf{x_{s1-2}}; \mathbf{y_{s1-2}})$, also measured in the 20th year.
3. Minimize Cold Well Damage Risk, $f_{2-1}(\mathbf{x_{s2-1}}; \mathbf{y_{s2-1}})$. Here, the geomechanical stability assessment is formulated as a binary classification task. A system is classified as safe if the change in the slip tendency, $\Delta\phi$, is less than 4° and as failure otherwise. This binary formulation is adopted because engineering decisions often require discrete risk categorizations. The threshold

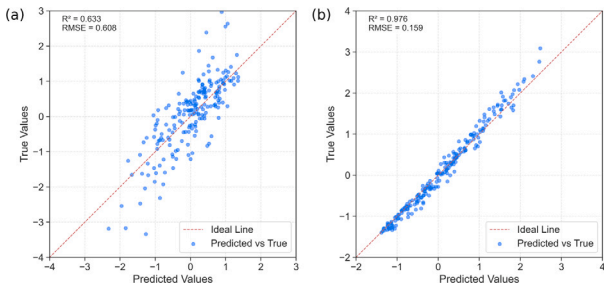

Fig. 20. Performance of Proxy Models: (a) Regression results for TRE f_{1-1}. (b) Regression results for AHP f_{1-2}. The scatter plot compares predicted values with true values, with the dashed red line representing the ideal 1:1 relationship.

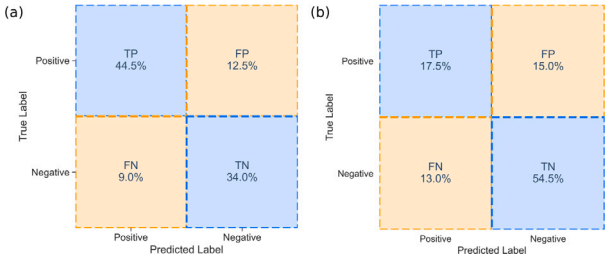

Fig. 21. Classification Performance: (a) Confusion matrix for cold well stability classification f_{2-1} and (b) Confusion matrix for caprock stability classification f_{2-2}. In each matrix, TP (true positives), FP (false positives), FN (false negatives), and TN (true negatives) are indicated.

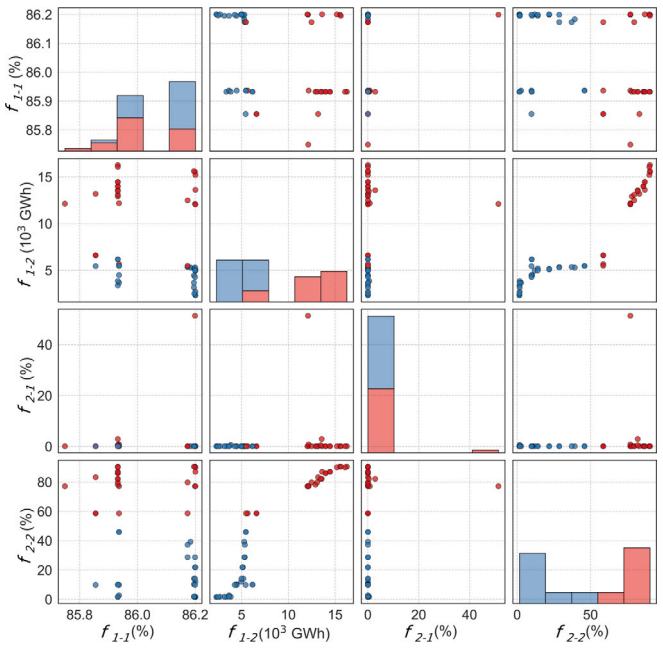

Fig. 22. Multi-objective Pareto optimization results, illustrating the trade-offs among thermal efficiency, heat production, and system stability. Red markers indicate samples where stability metrics exceed the 50% threshold.

of $\Delta\phi = 4°$ is selected to balance the sample distribution and mitigate class imbalance during model training. It is important to note that this threshold primarily serves to enhance the robustness of the machine learning model rather than representing a direct physical failure criterion; future studies may further calibrate this value using empirical data.

4. Minimize Caprock Damage Risk, $f_{2-2}(\mathbf{x}_{\mathbf{s2-2}}; \mathbf{y}_{\mathbf{s2-2}})$, assessed using a similar binary classification based on the corresponding $\Delta\phi$ after hot water injection.

To reduce the computational burden of high-fidelity THM simulations during optimization, XGBoost surrogate models using the same dataset is employed for the sensitivity analysis. In constructing these surrogates, only the parameters with sensitivity values greater than 1 in each group are selected as input features. Two regression models predict the energy production metrics f_{1-1} and f_{1-2}, while two classification models assess the geomechanical risks f_{2-1} and f_{2-2} (with safety defined as $\Delta\phi < 4°$).

Fig. 20 presents scatter plots comparing surrogate predictions with high-fidelity simulation results for the regression models. The surrogate for f_{1-1} achieved an R^2 of 0.63 and an RMSE of 0.61, indicating moderate predictive performance for TRE, whereas the surrogate for f_{1-2} achieved an R^2 of 0.98 and an RMSE of 0.16, demonstrating excellent accuracy for AHP.

The performance of the XGBoost classifiers for the classification tasks is evaluated using confusion matrices that focus on key operational indicators (see Fig. 21). The cold well damage risk model, f_{2-1}, achieves a true positive rate (TPR) of 83.3% (calculated as $\frac{45\%}{45\%+9\%}$), demonstrating its strong capability in detecting hazardous conditions while minimizing the risk of overlooking critical failures. In contrast, the caprock damage risk model, f_{2-2}, exhibits a safety-first characteristic with a TPR of 57.4% (computed as $\frac{17.5\%}{17.5\%+13\%}$) and a true negative rate (TNR) of 78.4% (computed as $\frac{54.5\%}{54.5\%+15\%}$), thereby prioritizing the minimization of undetected caprock failures even if it results in a higher rate of false alerts. Overall, these performance metrics indicate that both surrogate classifiers effectively fulfill their intended objectives of reliably identifying hazardous conditions for their targets.

Overall, these validation results indicate that the surrogate models capture the key behaviors of the high-fidelity THM simulations with acceptable accuracy. Consequently, they are well-suited for integration into the subsequent multi-objective optimization framework, which will identify design solutions that balance enhanced energy production with reduced geomechanical risk.

3.3.2. Pareto optimization and trade-off analysis

In our multi-objective optimization framework, the problem is defined with three design variables: injection rate, warm well injection temperature, and cold well injection temperature ($\mathbf{x}$) with lower and upper bounds specified in Table 1. A fixed geological parameter vector from the benchmark model is provided as constant input; notely, the input and output combinations for each objective are determined based on parameter sensitivity.

To efficiently explore the trade-offs among these four competing objectives, the NSGA-II algorithm is employed. A population of 50 candidate solutions is evolved over 1000 iterations to form the Pareto front. In each generation, candidate designs are evaluated using the developed XGBoost surrogate models, which approximate the high-fidelity THM simulation outputs at a fraction of the computational cost.

Fig. 22 shows the Pareto fronts obtained from the multi-objective optimization, which simultaneously considers thermal efficiency, heat production, and geomechanical risks. Notably, two objectives f_{1-1} and f_{2-1} exhibit significant improvements in the optimized solutions. In particular, optimized f_{1-1} values increase TRE from approximately 85% to 86%, while nearly all solutions achieve a cold well risk f_{2-1} below 1%. In contrast, the distributions for f_{1-2} (AHP, ranging from 1 to 17×10^3 GWh) and f_{2-2} (Caprock Damage Risk, spanning 0% to 100%) remain broad.

This divergence in behavior arises from the distinct influence of the sensitive parameters. The f_{1-1} metric is predominantly affected by the injection rate, which also supports maximizing f_{1-2}; hence,

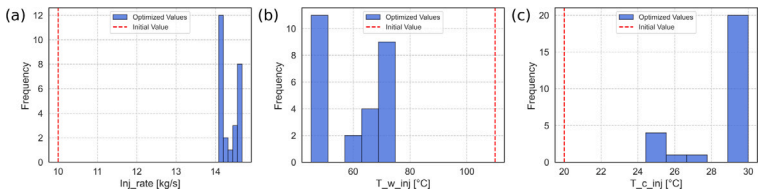

Fig. 23. Distribution of optimized parameter values compared to initial values. The blue bars represent the frequency of optimized values, while the red dashed lines indicate the initial values. (a) Injection rate, (b) warm well injection temperature, and (c) cold well injection temperature.

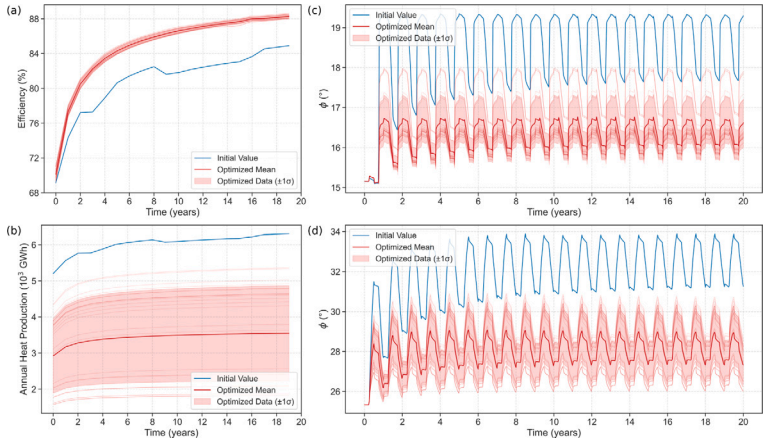

Fig. 24. Optimized performance indicators: (a) TRE, (b) AHP, (c) Cold Well ϕ, and (d) Caprock ϕ. In each plot, the blue line represents the benchmark model value, the fine red lines show the individual values of the optimized samples, and the thick red line indicates the mean of the optimized solutions.

there is little trade-off between these two objectives as the optimization drives f_{1-1} to its optimum. In contrast, f_{2-1} is mainly sensitive to the cold well injection temperature, a parameter with limited impact on the other objectives, allowing its risk to be effectively minimized. Conversely, f_{1-2} and f_{2-2} form a critical trade-off pair: higher injection temperatures boost AHP but also increase caprock damage risk. This inverse relationship is evident in the Pareto front as shown in Fig. 22, where designs that maximize heat production inevitably come at the expense of increased risk. Achieving greater system safety thus requires a compromise on the maximum attainable heat production.

To enforce safety constraints, we exclude all solutions for which the damage probability of either the cold well or the caprock exceeds 50% (as indicated by the red markers in Fig. 22). This filtering reduces the solution set from 50 to 26 candidates. Notably, the eliminated (unsafe) solutions exhibit substantially higher AHP (approximately 6–17 $\times 10^3$ GWh) compared to a maximum of about 6×10^3 GWh among the safe designs. Overall, the Pareto analysis elucidates the inherent trade-offs between energy output and geomechanical safety, providing valuable insights for selecting optimal design solutions that balance these competing objectives.

3.3.3. Optimized parameter distribution and full-model validation

Fig. 23 shows the statistical distributions of the three operational parameters among the 26 safe candidate solutions. The analysis reveals that the injection rate shifts from the benchmark value of 10 kg/s to a concentrated range around 14–15 kg/s, which aligns with DGSA findings that a higher injection rate enhances heat production efficiency by enabling rapid thermal charging of the reservoir. In contrast, the optimized warm well injection temperature decreases markedly from 110 °C to a range between 50 °C and 70 °C, reflecting a deliberate trade-off aimed at mitigating thermal stresses and improving caprock safety. Furthermore, the cold well injection temperature increases from the benchmark value of 20 °C to approximately 28 °C, thereby reducing the thermal gradient between the injected fluid and the reservoir to enhance overall system stability.

To verify the reliability of the surrogate-based optimization framework, a subset of the optimized designs was re-simulated using the full THM model. Fig. 24 presents the evolution curves for key performance indicators from these high-fidelity simulations. Although direct numerical comparisons between the surrogate predictions and full-model outcomes are not always exact-owing in part to the moderate accuracy of the f_{1-1} regression model (with $R^2 = 0.633$) which tends to underestimate heat production efficiency at higher values-the overall trends clearly indicate a substantial improvement in system performance. For instance, while the benchmark model exhibits a heat production efficiency (f_{1-1}) of approximately 85%, the optimized designs achieve around 88% according to the high-fidelity simulations. Similarly, although candidate solutions could theoretically reach AHP (f_{1-2}) values as high as $6{\times}10^3$ GWh, the safety-constrained designs yield a mean AHP of approximately 3.5×10^3 GWh, with the maximum value around 5.3×10^3 GWh. Moreover, the re-simulated geomechanical indicators (f_{2-1} and f_{2-2}) reveal significantly lower slip tendency in both the cold well and caprock regions compared to the benchmark model, confirming enhanced stability. In particular, the average maximum slip tendency in the caprock region is reduced to 29° in the candidate designs from 34° in the benchmark, further indicating improved caprock stability. These validation results demonstrate that the surrogate-based optimization framework reliably improves both energy efficiency and geomechanical safety, thereby substantiating its practical value in guiding the design of HT-ATES systems.

It should be noted that our optimization is performed under the assumption that the geological parameters are fixed for a given site. In practice, comprehensive site characterization typically determines these parameters, which remain largely unchanged over the operational lifespan of the system. By concentrating on controllable operational variables, our approach addresses the most actionable aspects of system design. This focus ensures that the resulting improvements in energy efficiency and geomechanical safety are both realistic and directly applicable within the specific geological context of the HT-ATES system.

4. Discussion

In this study, we present a coupled thermo-hydro-mechanical (THM) model integrated with distance-based generalized sensitivity analysis (DGSA) and a multi-objective optimization framework to investigate and optimize the performance and stability of high-temperature aquifer thermal energy storage (HT-ATES) systems. Our key findings indicate that the sensitive parameters identified by DGSA play a decisive role in explaining the failures observed in field projects, such as those at Utrecht University and in Zwammerdam [10,34]. Specifically, lower injection rates, combined with high reservoir permeability in coarse-grained aquifers and the influence of regional groundwater flow, contribute to a reduced TRE. In addition, our analysis provides new insights into mechanical stability by demonstrating that the thermo-mechanical coupling at both the cold well and the caprock, often neglected in conventional ATES designs, poses distinct challenges for HT-ATES. These findings underscore the limitations of traditional design paradigms treating thermal and mechanical processes separately. To address these interdependencies, our framework uniquely embeds DGSA based on the THM model dataset to prioritize key parameters, thereby enabling the NSGA-II algorithm to systematically explore the trade-offs between maximizing heat production and maintaining geomechanical stability. This integrated approach offers detailed guidance for designing systems that balance energy output with safety considerations.

This methodological advancement addresses two key gaps in conventional HT-ATES design: (1) the limitations of traditional sensitivity analysis methods, such as Sobol indices [35], in disentangling complex parameter interactions in coupled THM systems, and (2) the oversimplification inherent in single-objective optimization approaches that prioritize energy output at the expense of geomechanical safety [36]. By using DGSA, we overcome variance-based methods linearity assumptions, clustering system responses to identify dominant parameters and their interdependencies. For instance, DGSA reveals that the interplay between injection rate and reservoir properties, such as heat capacity and permeability, significantly enhances TRE-a relationship that remained obscured in earlier studies using more simplified modeling approaches. Our approach expands the uncertainty space by incorporating 19 parameters and selecting the sensitive ones via DGSA for surrogate model development. These surrogate models achieve an R^2 of approximately 97.6% in predicting heat production, outperforming earlier proxy models built on fewer than 10 parameters. [37]. Given that our study accounts for greater parameter uncertainty and a wider range of system responses, this high predictive accuracy substantiates the feasibility of our DGSA-based parameter selection and demonstrates that our method provides a more robust characterization of system behavior Furthermore, our NSGA-II-based multi-objective optimization framework transcends the limitations of conventional single-criterion approaches by generating Pareto-optimal solutions that quantify the trade-off between maximizing AHP and minimizing caprock failure probability. As a result, compared to a benchmark model that exhibits a TRE of approximately 85% and a caprock slip tendency of 34°, our optimized designs achieve around 88% efficiency and reduce the caprock slip tendency to 29°. This mirrors recent advances in geothermal reservoir optimization while extending them through the incorporation of DGSA-guided parameter screening, which accelerates convergence and ensures a focused exploration of the design space. Crucially, the integration of DGSA with NSGA-II establishes a novel workflow that prioritizes sensitive parameters, thereby enabling an efficient and systematic balance between performance and safety in HT-ATES systems. To our knowledge, this work represents one of the first attempts to achieve such a closed-loop integration of sensitivity analysis and multi-objective optimization in subsurface thermal energy storage, offering a replicable paradigm for addressing the inherent challenges of complex geoengineering systems.

The findings of this study provide actionable recommendations for HT-ATES engineering practice. In particular, designers should prioritize the control of DGSA-identified sensitive parameters. Practically, operational parameters should be adjusted within the constraints imposed by known geological conditions [24]. Next, continuous monitoring of pressure and temperature gradients at critical zones (such as cold wells and caprock interfaces) is recommended to detect early signs of stress accumulation and potential system instability. Furthermore, the integrated DGSA-optimization framework is not confined to HT-ATES alone; it can be adapted to other subsurface systems governed by coupled thermo-hydro-mechanical processes, such as enhanced geothermal reservoirs or carbon sequestration projects. By focusing on parameter interdependencies instead of fixed thresholds, this approach enables flexible adaptation to diverse geological settings, provided that site-specific data are used to inform the initial sensitivity screening. Ultimately, this methodology offers a transferable paradigm for optimizing the trade-offs between performance and safety in complex geoengineering systems, thereby bridging the gap between theoretical modeling and field-scale implementation.

While this study provides critical insights into HT-ATES design, several limitations warrant consideration. First, the 2D model does not capture fully resolve three-dimensional flow dynamics and stress heterogeneity, potentially underestimating lateral thermal dispersion and fracture-induced preferential pathways. Second, the assumption of homogeneous reservoir properties overlooks the impacts of geological heterogeneities (such as lithological layering, spatially variable permeability, and unmodeled fracture networks) on thermo-hydro-mechanical responses. Third, the exclusion of chemical processes, such as mineral dissolution and precipitation, limits the model's capability to predict long-term property alterations triggered by fluid-rock interactions. Consequently, porosity and permeability changes due to geochemical reactions are not captured. Lastly, although our surrogate models achieve a reasonable level of accuracy while offering significant computational efficiency, they inevitably introduce some uncertainties when approximating the complex coupled multi-physics behaviors, leaving room for further improvement in predictive performance.

Regarding heat loss, our model employs lateral boundary conditions that eliminate horizontal pressure gradients, thereby preventing convective heat loss due to fluid flow. Thus, heat loss is mainly by conduction to the caprock and basement. While this approach is widely used in theoretical analyses [5] and provides an overall estimate of system performance under high-temperature conditions, buoyancy-driven and lateral convective heat losses-driven by density variations or regional groundwater flow-may significantly reduce TRE in real-world ATES systems [38].

Future research should focus on developing 3D thermo-hydro-mechanical–chemical (THMC) models that incorporate heterogeneous geological features and realistic boundary conditions. In addition, coupling such 3D THMC models with advanced surrogate modeling techniques (such as physics-informed neural networks) could further enhance the robustness and generalizability of the optimization framework. Furthermore, extending this framework to other subsurface systems governed by multi-physics interactions would rigorously test its applicability while fostering cross-disciplinary innovation. Addressing these challenges will advance the design of sustainable geoenergy systems that holistically balance efficiency, safety, and long-term operational stability.

5. Conclusion

Our study demonstrates that an integrated THM modeling approach combined with DGSA and NSGA-II optimization offers a robust framework for enhancing the energy performance and geomechanical safety of HT-ATES systems. The results of our analysis are summarized as follows:

- The benchmark model demonstrates that cyclic thermal loading induces potential instability risks at both the cold well and caprock.
- Sensitivity analysis reveals that dominant parameters-such as injection rate, warm well injection temperature, reservoir thermal expansion coefficient, heat capacity, and permeability-critically control thermal recovery efficiency and geomechanical stability.
- These parameters exhibit inherent trade-offs, as higher injection temperatures enhance energy density while amplifying thermal stresses, whereas lower temperatures improve stability at the cost of reduced thermal output.
- The proposed optimization framework successfully reconciles these competing objectives, enabling designs that maximize heat production while maintaining mechanical integrity under realistic subsurface conditions.

CRediT authorship contribution statement

Le Zhang: Writing – original draft, Visualization, Software, Methodology, Conceptualization. **Zerui Mi:** Writing – original draft, Visualization, Software. **Wenzhuo Cao:** Writing – review & editing, Software. **Liyuan Liu:** Writing – review & editing, Methodology. **Luka Tas:** Writing – review & editing, Software, Conceptualization. **Thomas Hermans:** Writing – review & editing, Resources, Funding acquisition.

Declaration of competing interest

The authors declare that they have no known competing financial interests or personal relationships that could have appeared to influence the work reported in this paper.

Acknowledgments

This work was supported by the Bilateral Cooperation Project between Flanders and China (grant number G0E5222N) and Research Foundation Flanders (grant number: 1SH0M24N), This study is also part of the strategic basic research project DIAMONDS funded by the Research Foundation-Flanders (FWO) and the Flemish Government and the project DIAMONDS (grant number S001324N). And the National Natural Science Foundation of China (Grant Nos. 52278326, 52311530070, and 52004015), the Beijing Natural Science Foundation (Grant No. JQ21028).

Appendix A. Validation of the THM coupled model

To demonstrate the reliability of our thermo-hydro-mechanical (THM) coupling, we reproduce the classical analytical solution of [39, 40] for the instantaneous cooling of a circular wellbore in an infinite, water-saturated rock.

A square domain encloses a central borehole of radius $R = 0.10$ m (Fig. A.25). Roller supports are imposed on the left and bottom edges, while far-field stress, pore pressure, and temperature remain fixed at their initial values on the other boundaries. At $t = 0$, the borehole wall temperature is instantaneously reduced from 200 °C to 80 °C.

Initially, the solid skeleton has zero displacement and zero stress; the pore pressure is uniform $p_0 = 0$ MPa; and the temperature is uniform $T_0 = 200$ °C. Mechanically, roller constraints are applied on the outer edges and the borehole wall is stress-free. Hydraulically, $p = 0$ MPa is prescribed at both the borehole and the far-field boundaries. Thermally, Dirichlet conditions of 200 °C (far-field) and 80 °C (borehole wall) are enforced.

Table A.2 lists the mechanical and thermal parameters used in the validation. Thermal conductivity and Biot's coefficient are converted from the original source.

Numerical results for temperature, pore pressure, radial stress, and tangential stress were sampled along the radial line AB (Fig. A.25) and plotted against the normalized distance r/R. Fig. A.26 shows close agreement between numerical markers and analytical lines, with discrepancies below 5% in all fields. This confirms the accuracy and robustness of our coupled THM implementation.

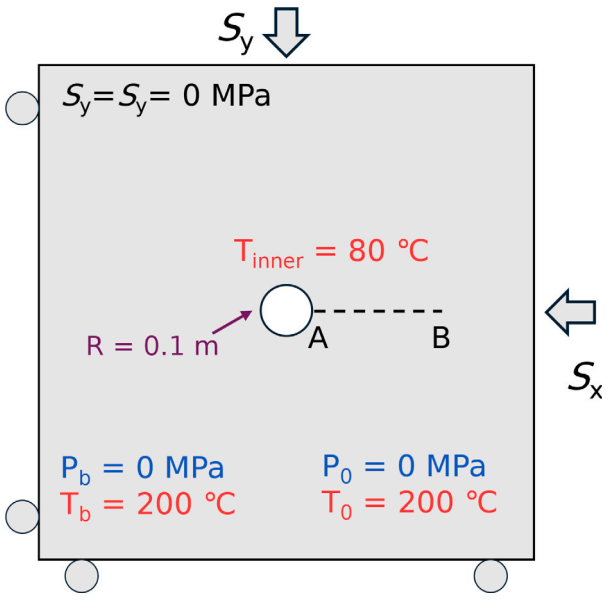

Fig. A.25. Schematic of the validation domain: borehole radius R, roller constraints (left/bottom), and prescribed far-field conditions.

Appendix B. DGSA mathematical details

This appendix provides the detailed mathematical derivations and formulas for the DGSA approach used in Section 3.2.

B.1. First-order sensitivity index

Initially, this method divides outputs into several clusters using a distance-based clustering approach. Let X be a model parameter and C the number of clusters. The normalized first-order sensitivity index is defined as:

$$S(X) = \frac{1}{C}\sum_{c=1}^{C}\hat{d}_c = \frac{1}{C}\sum_{c=1}^{C}\frac{d_{L1}\left(F(X),\, F(X \mid c)\right)}{\check{d}_a^c}, \tag{B.1}$$

where

$$\hat{d}_c = \frac{d_{L1}\left(F(X),\, F(X \mid c)\right)}{\check{d}_a^c}, \quad d_{L1}\left(F(X),\, F(X \mid c)\right) = \int \left|F_X(x) - F_{X|c}(x)\right| dx,$$

$\check{d}_a^c$ is the ath quartile of the within-cluster distances for cluster c, with $a = 0.95$ in this study. Here, $F(X)$ denotes the CDF of the parameter X over all samples, and $F(X \mid c)$ the CDF conditioned on membership in cluster c. If $S(X) > 1$, parameter X is considered sensitive [41].

B.2. Second-order (conditional) sensitivity index

DGSA can also compute conditional (second-order) sensitivities to account for interactions between two parameters X_i and X_j. The conditional sensitivity $S(X_i \mid X_j)$ is given by:

$$S(X_i \mid X_j) = \frac{1}{C}\frac{1}{L}\sum_{c=1}^{C}\sum_{l=1}^{L}\hat{d}_{c,i|j,l}, \tag{B.2}$$

where

$$\hat{d}_{c,i|j,l} = \frac{d_{L1}\left(F(X_i \mid j = l),\, F(X_i \mid c)\right)}{\hat{\check{d}}_{c,i|j,l}(a)}, \quad l = 1, \ldots, L,\ c = 1, \ldots, C.$$

Table A.2
Material and fluid parameters for model validation.

Parameter	Symbol	Value
Elastic modulus	E	37.5 GPa
Poisson's ratio	ν	0.25
Porosity	ϕ	0.01
Permeability	k	4×10^{-19} m^2
Biot's coefficient	α	0.443
Rock density	ρ_r	2600 kg/m^3
Thermal conductivity (rock)	λ_r	10.48 W/(m K)
Thermal expansion (rock)	β_r	8.16×10^{-6} K^{-1}
Heat capacity (rock)	c_r	790 J/(kg K)
Fluid density	ρ_f	1000 kg/m^3
Heat capacity (fluid)	c_f	4200 J/(kg K)
Thermal conductivity (fluid)	λ_f	258.7 W/(m K)
Fluid viscosity	μ_f	3.55×10^{-4} Pa s

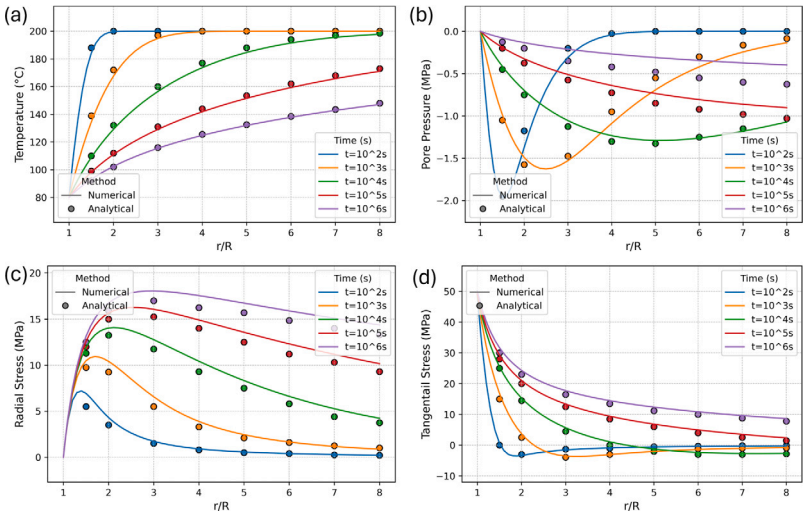

Fig. A.26. Comparison of numerical (markers) and analytical (lines) solutions for: (a) temperature; (b) pore pressure; (c) radial stress; (d) tangential stress. Positive values denote compression.

Here, $F(X_i \mid j = l)$ is the CDF of X_i given that X_j takes its lth level, and $\widehat{\widehat{d}}_{c,i|j,l}(a)$ denotes the ath quartile of the within-cluster distances for X_i in cluster c when X_j is fixed at level l.

Data availability

The data that support the findings of this study have been deposited in the 4TU. ResearchData repository, https://doi.org/10.4121/5770abff-df68-4e9e-900c-b3add1e3d210.

References

[1] Yang T, Liu W, Kramer GJ, Sun Q. Seasonal thermal energy storage: A techno-economic literature review. Renew Sustain Energy Rev 2021;139:110732. http://dx.doi.org/10.1016/j.rser.2021.110732.

[2] Shah M, Prajapati M, Yadav K, Sircar A. A comprehensive review of geothermal energy storage: Methods and applications. J Energy Storage 2024;98:113019. http://dx.doi.org/10.1016/j.est.2024.113019.

[3] Fleuchaus P, Godschalk B, Stober I, Blum P. Worldwide application of aquifer thermal energy storage–a review. Renew Sustain Energy Rev 2018;94:861–76. http://dx.doi.org/10.1016/j.rser.2018.06.057.

[4] Tas L, Simpson D, Hermans T. Assessing the potential of low-transmissivity aquifers for aquifer thermal energy storage systems: a case study in Flanders (Belgium). Hydrogeol J 2023;31(8):2363–80. http://dx.doi.org/10.1007/s10040-023-02696-5.

[5] Tas L, Hartog N, Bloemendal M, Simpson D, Robert T, Thibaut R, et al. Efficiency and heat transport processes of low-temperature aquifer thermal energy storage systems: new insights from global sensitivity analyses. Geotherm Energy 2025;13(1):1–27. http://dx.doi.org/10.1186/s40517-024-00326-1.

[6] Bloemendal M, Jaxa-Rozen M, Olsthoorn T. Methods for planning of ates systems. Appl Energy 2018;216:534–57. http://dx.doi.org/10.1016/j.apenergy.2018.02.068.

[7] Fleuchaus P, Schüppler S, Bloemendal M, Guglielmetti L, Opel O, Blum P. Risk analysis of high-temperature aquifer thermal energy storage (ht-ates). Renew Sustain Energy Rev 2020;133:110153. http://dx.doi.org/10.1016/j.rser.2020.110153.

[8] Daniilidis A, Mindel JE, De Oliveira Filho F, Guglielmetti L. Techno-economic assessment and operational Co2 emissions of high-temperature aquifer thermal energy storage (ht-ates) using demand-driven and subsurface-constrained dimensioning. Energy 2022;249:123682. http://dx.doi.org/10.1016/j.energy.2022.123682.

[9] De Schepper G, Paulus C, Bolly P-Y, Hermans T, Lesparre N, Robert T. Assessment of short-term aquifer thermal energy storage for demand-side management perspectives: Experimental and numerical developments. Appl Energy 2019;242:534–46. http://dx.doi.org/10.1016/j.apenergy.2019.03.103.

[10] Drijver B, Bakema G, Oerlemans P. State of the art of ht-ates in the Netherlands. In: European geothermal congress: proceedings. 2019, https://europeangeothermalcongress.eu/wp-content/uploads/2019/07/289.pdf.

[11] Szklarz S, Dinkelman D, Khoshnevis Gargar N, Boullenger B, Peters E, Barros E, et al. Ensemble-based assisted history matching of dts monitoring data in ht-ates systems: application to a real-life case study. Geotherm Energy 2024;12(1):46. http://dx.doi.org/10.1186/s40517-024-00329-y.

[12] McLing TL, Dobson P, Jin W, Spycher N, Doughty C, Neupane GH, et al. Dynamic earth energy storage: terawatt-year, grid-scale energy storage using planet earth as a thermal battery (geotes): phase i project. Tech. rep., Idaho National Lab.(INL), Idaho Falls, ID (United States; 2022, https://www.osti.gov/biblio/1885826.

[13] Vardon P, van der Schans M, Koulidis A, Grubben T, Beernink S, Bloemendal M. High-temperature aquifer thermal energy storage (ht-ates) system for research development and demonstration on the tu delft campus. Tech. rep., Copernicus Meetings; 2024, http://dx.doi.org/10.5194/egusphere-egu24-14989.

[14] Liu L, Jin J, Liu J, Cheng W, Zhao M, Luo S, et al. Mechanical properties of sandstone under in-situ high-temperature and confinement conditions. Int J Miner Met Mater 2025;1–10. http://dx.doi.org/10.1007/s12613-024-3047-9.
[15] Zhang Z-K, Lai J-X, p. Song Z, Xie Y-L, l. Qiu J, Cheng Y, et al. Investigating fracture response characteristics and fractal evolution laws of pre-holed hard rock using infrared radiation: Implications for construction of underground works. Tunn Undergr Space Technol 2025;161:106594. http://dx.doi.org/10.1016/j.tust.2025.106594.
[16] Liu L, Luo S, Elsworth D, Liu K, Luo Y, Ji H, et al. Linking evolution of heterogeneous microstructure and rheology of granite to 1000° c. J Rock Mech Geotech Eng 2025. http://dx.doi.org/10.1016/j.jrmge.2025.03.006.
[17] Liu Y, Liang Y, Ma Y, Liu J, Elsworth D, Gan Q. Dynamic evolution of reservoir permeability and deformation in geothermal battery energy storage using abandoned mines. Rock Mech Bull 2025;4(1):100155. http://dx.doi.org/10.1016/j.rockmb.2024.100155.
[18] Zhang N, Luo Z, Chen Z, Liu F, Liu P, Chen W, et al. Thermal–hydraulic–mechanical–chemical coupled processes and their numerical simulation: a comprehensive review. Acta Geotech 2023;18(12):6253–74. http://dx.doi.org/10.1007/s11440-023-01976-4.
[19] Parisio F, Vilarrasa V, Wang W, Kolditz O, Nagel T. The risks of long-term re-injection in supercritical geothermal systems. Nat Commun 2019;10(1):4391. http://dx.doi.org/10.1038/s41467-019-12146-0.
[20] Stricker K, Egert R, Schill E, Kohl T. Risk of surface movements and reservoir deformation for high-temperature aquifer thermal energy storage (ht-ates). Geotherm Energy 2024;12(1):4. http://dx.doi.org/10.1186/s40517-024-00283-9.
[21] Hermans T, Lesparre N, De Schepper G, Robert T. Bayesian evidential learning: a field validation using push-pull tests. Hydrogeol J 2019;27(5):1661–72. http://dx.doi.org/10.1007/s10040-019-01962-9.
[22] Cao W, Durucan S, Shi J-Q, Korre A, Ratouis T, Hjörleifsdóttir V. Geothermal fluid extraction and injection-related fracture slip susceptibility and seismicity in naturally fractured rocks. Int J Rock Mech Min Sci 2024;183:105939. http://dx.doi.org/10.1016/j.ijrmms.2024.105939.
[23] Wang K, Liu Z, Zeng T, Wang F, Shen W, Shao J. Performance of enhanced geothermal system with varying injection-production parameters and reservoir properties. Appl Therm Eng 2022;207:118160. http://dx.doi.org/10.1016/j.applthermaleng.2022.118160.
[24] Zhang L, Dieudonné A-C, Daniilidis A, Dong L, Cao W, Thibaut R, et al. Thermo-hydro-mechanical modeling of geothermal energy systems in deep mines: Uncertainty quantification and design optimization. Appl Energy 2025;377:124531. http://dx.doi.org/10.1016/j.apenergy.2024.124531.
[25] Hermans T, Nguyen F, Klepikova M, Dassargues A, Caers J. Uncertainty quantification of medium-term heat storage from short-term geophysical experiments using Bayesian evidential learning. Water Resour Res 2018;54(4):2931–48. http://dx.doi.org/10.1002/2017WR022135.
[26] Fenwick D, Scheidt C, Caers J. Quantifying asymmetric parameter interactions in sensitivity analysis: application to reservoir modeling. Math Geosci 2014;46:493–511. http://dx.doi.org/10.1007/s11004-014-9530-5.
[27] COMSOL. COMSOL multiphysics reference manual. 2024, URL https://doc.comsol.com/6.2/docserver/com.comsol.help.comsol/helpdesk/helpdesk.html.
[28] Tamizdoust MM, Ghasemi-Fare O. A fully coupled thermo-poro-mechanical finite element analysis to predict the thermal pressurization and thermally induced pore fluid flow in soil media. Comput Geotech 2020;117:103250. http://dx.doi.org/10.1016/j.compgeo.2019.103250.
[29] Zhang Y, Gao X, Sun C, Ye C, Gong Y, Kong Y, et al. Thermal performance and analysis of high-temperature aquifer thermal energy storage based on a practical project. J Energy Storage 2024;82:110399. http://dx.doi.org/10.1016/j.est.2023.110399.
[30] Perzan Z, Babey T, Caers J, Bargar J, Maher K. Local and global sensitivity analysis of a reactive transport model simulating floodplain redox cycling. Water Resour Res 2021;57(12):e2021WR029723. http://dx.doi.org/10.1029/2021wr029723.
[31] Park J, Yang G, Satija A, Scheidt C, Caers J. Dgsa: A matlab toolbox for distance-based generalized sensitivity analysis of geoscientific computer experiments. Comput Geosci 2016;97:15–29. http://dx.doi.org/10.1016/j.cageo.2016.08.021.
[32] Yu R, Zhang K, Ramasubramanian B, Jiang S, Ramakrishna S, Tang Y. Ensemble learning for predicting average thermal extraction load of a hydrothermal geothermal field: A case study in Guanzhong Basin China. Energy 2024;296:131146. http://dx.doi.org/10.1016/j.energy.2024.131146.
[33] Deb K, Pratap A, Agarwal S, Meyarivan T. A fast and elitist multiobjective genetic algorithm: Nsga-ii. IEEE Trans Evol Comput 2002;6(2):182–97. http://dx.doi.org/10.1109/4235.996017.
[34] Kallesøe AJ, Vangkilde-Pedersen T. Underground thermal energy storage (utes) – state-of-the-art, example cases and lessons learned. Tech. rep., GEOTHERMICA – ERA NET Cofund Geothermal, hEATSTORE project report, 130 pp + appendices; 2019.
[35] Song X, Zhang J, Zhan C, Xuan Y, Ye M, Xu C. Global sensitivity analysis in hydrological modeling: Review of concepts, methods, theoretical framework, and applications. J Hydrol 2015;523:739–57. http://dx.doi.org/10.1016/j.jhydrol.2015.02.013.
[36] Bloemendal M, Hartog N. Analysis of the impact of storage conditions on the thermal recovery efficiency of low-temperature ates systems. Geothermics 2018;71:306–19. http://dx.doi.org/10.1016/j.geothermics.2017.10.009.
[37] Wang J, Tan X, Zhao Z, Chen J, He J, Shi Q. Coupled thermo-hydro-mechanical modeling on geothermal doublet subject to seasonal exploitation and storage. Energy 2024;293:130650. http://dx.doi.org/10.1016/j.energy.2024.130650.
[38] Beernink S, Hartog N, Vardon PJ, Bloemendal M. Heat losses in ates systems: the impact of processes, storage geometry and temperature. Geothermics 2024;117:102889. http://dx.doi.org/10.1016/j.geothermics.2023.102889.
[39] Ghassemi A, Zhang Q. A transient fictitious stress boundary element method for porothermoelastic media. Eng Anal Bound Elem 2004;28(11):1363–73. http://dx.doi.org/10.1016/j.enganabound.2004.05.003.
[40] Liu L, Li Y, Cao W, Wang T, Zhang L, Feng X. Coupled thermo-hydro-mechanical-damage modeling of cold-water injection in deep geothermal reservoirs. J Rock Mech Geotech Eng 2025. http://dx.doi.org/10.1016/j.jrmge.2025.06.002.
[41] Scheidt C, Li L, Caers J. In: Quantifying uncertainty in subsurface systems, vol. 236, John Wiley & Sons; 2018, http://dx.doi.org/10.1002/9781119325888.ch8.